

HI discs of L_* galaxies as probes of the baryonic physics of galaxy evolution

Jindra Gensior¹*, Robert Feldmann¹, Marta Reina-Campos^{2,3}, Sebastian Trujillo-Gomez^{4,5}, Lucio Mayer¹, Benjamin W. Keller⁶, Andrew Wetzel⁷, J. M. Diederik Kruijssen^{8,9}, Philip F. Hopkins¹⁰ and Jorge Moreno^{11,12}

¹*Department of Astrophysics, University of Zurich, Winterthurerstrasse 190, 8057 Zürich, Switzerland*

²*Department of Physics & Astronomy, McMaster University, 1280 Main Street West, Hamilton, L8S 4M1, Canada*

³*Canadian Institute for Theoretical Astrophysics (CITA), University of Toronto, 60 St George St, Toronto, M5S 3H8, Canada*

⁴*Astroinformatics Group, Heidelberg Institute for Theoretical Studies, Schloss-Wolfsbrunnengasse 35, 69118 Heidelberg, Germany*

⁵*Astronomisches Rechen-Institut Zentrum für Astronomie der Universität Heidelberg, Mönchhofstraße 12-14, 69120 Heidelberg, Germany*

⁶*Department of Physics and Materials Science, University of Memphis, 3720 Alumni Avenue, Memphis, TN 38152, USA*

⁷*Department of Physics & Astronomy, University of California, Davis, CA 95616, USA*

⁸*Technical University of Munich, School of Engineering and Design, Department of Aerospace and Geodesy, Chair of Remote Sensing Technology, Arcisstr. 21, 80333 Munich, Germany*

⁹*Cosmic Origins Of Life (COOL) Research DAO, coolresearch.io*

¹⁰*California Institute of Technology, TAPIR, Mailcode 350-17, Pasadena, CA 91125, USA*

¹¹*Department of Physics and Astronomy, Pomona College, Claremont, CA 91711, USA*

¹²*Center for Computational Astrophysics, Flatiron Institute, 162 Fifth Avenue, New York, NY 10010, USA*

Accepted 2024 May 02. Received 2024 April 26; in original form 2023 September 30

ABSTRACT

Understanding what shapes the cold gas component of galaxies, which both provides the fuel for star formation and is strongly affected by the subsequent stellar feedback, is a crucial step towards a better understanding of galaxy evolution. Here, we analyse the HI properties of a sample of 46 Milky Way halo-mass galaxies, drawn from cosmological simulations (EMP-*Pathfinder* and FIREBOX). This set of simulations comprises galaxies evolved self-consistently across cosmic time with different baryonic sub-grid physics: three different star formation models [constant star formation efficiency (SFE) with different star formation eligibility criteria, and an environmentally-dependent, turbulence-based SFE] and two different feedback prescriptions, where only one sub-sample includes early stellar feedback. We use these simulations to assess the impact of different baryonic physics on the HI content of galaxies. We find that the galaxy-wide HI properties agree with each other and with observations. However, differences appear for small-scale properties. The thin HI discs observed in the local Universe are only reproduced with a turbulence-dependent SFE and/or early stellar feedback. Furthermore, we find that the morphology of HI discs is particularly sensitive to the different physics models: galaxies simulated with a turbulence-based SFE have discs that are smoother and more rotationally symmetric, compared to those simulated with a constant SFE; galaxies simulated with early stellar feedback have more regular discs than supernova-feedback-only galaxies. We find that the rotational asymmetry of the HI discs depends most strongly on the underlying physics model, making this a promising observable for understanding the physics responsible for shaping the interstellar medium of galaxies.

Key words: galaxies: evolution – galaxies: formation – galaxies: ISM – galaxies: star formation – ISM: structure

1 INTRODUCTION

The physics of star formation and stellar feedback present one of the largest uncertainties in our understanding of galaxy formation and evolution (e.g. Somerville & Davé 2015; Naab & Ostriker 2017; Crain & van de Voort 2023). An additional complication from a theoretical perspective is how to encode these small-scale processes in models for cosmological-scale simulations that cannot accurately resolve these scales.

On galactic scales, the star formation rate (SFR) surface density

is proportional to the (molecular) gas surface density (e.g. Kennicutt 1998; Bigiel et al. 2008; de los Reyes & Kennicutt 2019; Sun et al. 2023). Gas is converted into stars with an efficiency of ~ 1 per cent (e.g. Leroy et al. 2008; Krumholz et al. 2012) per free-fall time (t_{ff} , the time it would take for a gas cloud to collapse under its own self-gravity). However, there is growing evidence that the star formation efficiency (SFE) varies between galaxies (e.g. Utomo et al. 2018, Chevance et al. 2020, Kim et al. 2022, Sun et al. 2023), as well as within galaxies (e.g. Longmore et al. 2013; Kruijssen et al. 2014; Usero et al. 2015; Barnes et al. 2017; Querejeta et al. 2019). This suggests that the SFE per free-fall time (ϵ_{ff}) is not constant (as is often assumed for the sub-grid modelling of star formation), but depends

* E-mail: jindra.gensior@uzh.ch

on properties of the local galactic environment on giant molecular cloud scales.

Analytic theory and high-resolution star formation simulations of molecular clouds in turbulent boxes suggest that ϵ_{ff} depends on the turbulent properties of the gas. Specifically, on the virial parameter (α_{vir} , the ratio of gravitational potential to turbulent kinetic energy of a cloud) and the turbulent Mach number ($\mathcal{M} = \sigma/c_s$ the ratio of the turbulent velocity dispersion to the sound speed) of the gas (e.g. Krumholz & McKee 2005; Padoan & Nordlund 2011; Hennebelle & Chabrier 2011; Federrath & Klessen 2012; Burkhardt 2018). Such models can successfully explain the low star formation rate in the Milky Way (Evans et al. 2022) and are able to reproduce the suppressed star formation rates observed (e.g. Davis et al. 2014) in molecular gas-hosting early-type galaxies (e.g. Gensior et al. 2020; Kretschmer & Teyssier 2020; Gensior & Kruijssen 2021), something that constant ϵ_{ff} models struggle to accomplish.

The necessity of stellar feedback in regulating star formation and producing realistic galaxies resembling those observed in the (local) Universe has long been established (e.g. Somerville & Davé 2015; Naab & Ostriker 2017, for reviews). Stellar feedback is generally included via the effect of supernovae, and only some simulations include additional ‘early’ stellar feedback processes (i.e. all processes like winds, radiation pressure and photoelectric heating and photoionization by massive OB stars that act before the first supernova explodes). However, recent observations have highlighted the importance of the so-called early stellar feedback processes¹ in destroying molecular clouds (e.g. Chevance et al. 2022, Kim et al. 2022, Chevance et al. 2023 and simulations including early stellar feedback reproduce these short cloud lifetimes, e.g. Benincasa et al. 2020, Semenov et al. 2021, Keller et al. 2022). However, incorporating parametrisations of these processes into simulations seems to primarily affect the density structure of the interstellar medium (ISM) and subsequent outflow mass loading, rather than the global star formation rate (e.g. Stinson et al. 2013; Smith et al. 2021; Keller et al. 2022).

How these more empirically-motivated star formation and stellar feedback models affect galaxy properties when taking into account their highly non-linear interplay through the evolution across cosmic time has been tested for individual objects in cosmological zoom-in simulations (e.g. Kretschmer & Teyssier 2020; Nuñez-Castiñeira et al. 2021). However, a thorough exploration of their effects in a statistical sample of objects has yet to be carried out. Combining the *EMP-Pathfinder* (Reina-Campos et al. 2022) suite of cosmological zoom-in simulations and galaxies in the same halo mass range from the *FIREBOX* (Feldmann et al. 2023) cosmological volume puts us in an ideal position to do so. Between them, our data-set consists of galaxies simulated with three different star formation models (constant ϵ_{ff} with two different sets of criteria for making gas star-forming eligible, and a turbulence-based ϵ_{ff}) and two different stellar feedback models (only *FIREBOX* includes early stellar feedback). In this paper, we focus on analysing and comparing the HI properties of these galaxies at $z = 0$.

While molecular gas appears to be the predominant fuel for star formation (e.g. Tacconi et al. 2020, and references therein), HI plays an important role as a gas reservoir for future episodes of star formation (e.g. Popping et al. 2014; Wang et al. 2020; Saintonge & Catinella 2022). Furthermore, the HI discs of galaxies are strongly affected by

the resultant stellar feedback: supernovae drive turbulence, enhancing the velocity dispersion of the HI (e.g. Bacchini et al. 2020) and have the capacity to drive outflows and create massive holes in the HI disc (e.g. Silich & Tenorio-Tagle 2001; Boomsma et al. 2008; Orr et al. 2022). In addition to being intimately linked to both of the physical processes we are interested in, HI is a well-studied ISM tracer in the nearby universe. Data on the properties of HI discs are available through surveys such as the Westerbork HI survey of SPiral and irregular galaxies (WHISP; Swaters et al. 2002), The HI Nearby Galaxy Survey (THINGS; Walter et al. 2008), the *BLUEDISK* project (Wang et al. 2013), *xGASS* (Catinella et al. 2018) and the pilot surveys of the Square Kilometer Array (SKA) precursors, such as the MeerKAT International GHz Tiered Extragalactic Exploration (MIGHTEE; Jarvis et al. 2016) on MeerKAT and the Widefield ASKAP L-band Legacy All-sky Blind survey (WALLABY; Koribalski et al. 2020) on the Australian SKA Pathfinder (ASKAP). Therefore, HI (and the HI disc properties in particular) promise to be an excellent observable against which to compare the simulated galaxies in our sample and to make predictions for the (precursors of the) SKA.

The remainder of this paper is structured as follows. In Section 2 we introduce our sample of simulated galaxies and the baryonic physics with which the simulations were run. We present and discuss the properties of the HI discs of the galaxies in Section 3. In Section 4, we analyse the morphologies of the HI discs, quantified with the non-parametric morphological indicators Gini, Smoothness and Asymmetry. Moving beyond a descriptive analysis, we utilise random forest regressions to infer the (galaxy) properties most relevant to predict the different HI disc morphologies in Section 5. Finally, we conclude in Section 6.

2 THE SIMULATIONS

2.1 *EMP-Pathfinder*

EMP-Pathfinder is a suite of cosmological zoom-in simulations of L_* galaxies introduced in Reina-Campos et al. (2022), run with the moving-mesh code *AREPO* (Springel 2010; Weinberger et al. 2020) and the *EMP-Pathfinder* sub-grid physics implementation. Initial conditions match those of the *MOdelling Star cluster population Assembly In Cosmological Simulations within EAGLE* (*E-MOSAICS*; Pfeffer et al. 2018; Kruijssen et al. 2019) project and were drawn from the *EAGLE* Recal-L025N0752 DM-only periodic volume (Schaye et al. 2015). The *E-MOSAICS* initial conditions were selected solely for their halo mass, $11.85 < \log_{10}(M_{200}/M_{\odot}) < 12.48$, to represent present-day Milky Way-mass galaxies.

To match *E-MOSAICS*, *EMP-Pathfinder* has a baryonic mass resolution of $\sim 2.2 \times 10^5 M_{\odot}$, and $1 \times 10^6 M_{\odot}$ for the highest-resolution dark matter particles, which populate the 600 kpc of the simulation volume surrounding the central galaxy. Gas softening is adaptive, with a minimum gravitational softening length of $56.3 \text{ pc} h^{-1}$, which is comoving for the entire run. The Plummer-equivalent gravitational softening for stars and dark matter is fixed in comoving units until $z = 2$ (450 and $822 \text{ pc} h^{-1}$, respectively), and fixed to 175 and 320 pc, respectively at $z \leq 2$.

The *Grackle* chemistry and cooling library² (Smith et al. 2017) with the 6-species chemistry network is used to model the thermal state of the interstellar medium. Specifically, the tabulated metal cooling, non-equilibrium chemistry for H, H⁺, He, He⁺, He⁺⁺ and

¹ For brevity, we use this terminology throughout the remainder of the paper to refer to the wind, radiation pressure, photoelectric heating and photoionization feedback from massive OB stars.

² <https://grackle.readthedocs.io/>

electrons, and photoelectric heating and photoionization from the [Haardt & Madau \(2012\)](#) UV-Background, allow a self-consistent modelling of the multi-phase interstellar medium in the temperature range $10\text{--}10^9$ K.

An outstanding feature of EMP-*Pathfinder* relevant to this work is that it is a set of cosmological zoom-in simulations that evolved a suite of identical initial conditions with two different star formation sub-grid models, allowing us to study the effects that different sub-grid star-formation physics have when evolving galaxies self-consistently across cosmic time in a representative sample of Milky Way-halo mass galaxies rather than for individual objects. The fiducial subset of the sample (*Pathfinder*-cSFE), has $\epsilon_{\text{ff}} = 20$ per cent, while in *Pathfinder*-mffSFE the star formation efficiency per free-fall time depends on the turbulent state of the gas via the Mach number and the virial parameter. Specifically, the [Federrath & Klessen \(2012\)](#) multi-free-fall description of the [Krumholz & McKee \(2005\)](#) model is used, following [Kretschmer & Teysier \(2020\)](#). The SFE is given by:

$$\epsilon_{\text{ff}} = \frac{1}{2} \exp\left(\frac{3\sigma_s^2}{8}\right) \left[1 + \operatorname{erf}\left(\frac{\sigma_s^2 - s_{\text{crit}}}{\sqrt{2\sigma_s^2}}\right) \right], \quad (1)$$

where $\sigma_s = \ln(1 + 0.49M^2)$ is the the width of the turbulent density probability distribution function and s_{crit} is the lognormal critical density for star formation

$$s_{\text{crit}} = \ln \left[\alpha_{\text{vir}} \left(1 + \frac{2M^4}{1 + M^2} \right) \right]. \quad (2)$$

The velocity dispersion (and thus Mach number) and virial parameter are calculated on the cloud scale using the overdensity method of [Gensior et al. \(2020\)](#), which essentially performs an on-the-fly ‘cloud’ identification for each gas cell. Gas particles are eligible for star formation when their hydrogen number density exceeds 1 atom per cubic centimetre and their temperature is below 1.5×10^4 K. This high temperature threshold is necessitated by initialising the simulation with gas particles that have primordial metallicities. The gas thus cannot cool below $\sim 10^4$ K until the first stars have formed and subsequent supernovae and winds have enriched the remaining gas. However, once the the gas has been metal enriched, it can cool rapidly and stars form predominantly in gas with temperatures $\lesssim 200$ K. Star formation is treated stochastically, and the main impact of the turbulence-based SFE is that star formation preferentially occurs at (much) higher gas densities, compared to *Pathfinder*-cSFE. This will be discussed in more detail in a dedicated EMP-*Pathfinder* star formation paper (Gensior et al. in preparation). The stellar feedback channels included in EMP-*Pathfinder* are mass, metal, energy and momentum injection from supernovae of Type II and Type Ia, and winds from evolved (AGB) stars. Haloes were identified using a combination of the Friend-of-Friends (FoF; [Davis et al. 1985](#)) and SUBFIND algorithms ([Springel et al. 2001](#); [Dolag et al. 2009](#)).

2.2 FIREbox

FIREBOX ([Feldmann et al. 2023](#)) is a $(22.1 \text{ Mpc})^3$ cosmological volume simulation that is part of the Feedback In Realistic Environments (FIRE³) project. It was run with the meshless-finite-mass code GIZMO⁴ ([Hopkins 2015](#)) and the FIRE-2 ([Hopkins et al. 2018](#)) sub-grid

physics implementation. We use the fiducial FIREBOX run (FB1024) for our analysis. This simulation has a baryonic mass resolution of $6.4 \times 10^4 M_{\odot}$ and a dark matter mass resolution of $3.4 \times 10^5 M_{\odot}$. The fiducial FIREBOX and its next lower resolution re-run (FB512) bracket the mass resolution of EMP-*Pathfinder*, being a factor of 2 higher and lower respectively. We use the higher resolution FIREBOX, but note that our conclusions will not change when using the lower-resolution volume, due to the excellent convergence of the HI properties of FIREBOX (see e.g. online supplementary material in [Gensior et al. 2023b](#)). Gas particles have adaptive gravitational softening with a minimum Plummer-equivalent gravitational softening length of 1.5 pc (although the average softening length of star-forming gas is ~ 20 pc), the Plummer-equivalent softening lengths of stars and dark matter particles are 20 pc and 80 pc respectively. All softening lengths are comoving at $z \geq 9$, and fixed in physical units for $z \leq 9$.

The FIRE-2 sub-grid physics model naturally leads to a multiphase ISM, including the cold phase, using the [Hopkins et al. \(2014\)](#) heating and cooling rates which are valid for temperatures ranging from $10\text{--}10^9$ K and accounting for photoelectric heating and photoionization from the [Faucher-Giguère et al. \(2009\)](#) UV-Background. Star formation proceeds in gas above a density threshold of 300 atoms per cubic centimetre, that is self-gravitating ($\alpha_{\text{vir}} < 1$), Jeans unstable (Jeans mass lower than the gas particle mass), and molecular, with a star formation efficiency per free-fall time of 100 per cent. While differing from *Pathfinder*-mffSFE in the details of the numerical implementation and the behaviour at higher Mach numbers, the FIRE-2 star formation model is also motivated by turbulent star formation theory (see e.g. [Hopkins et al. 2013, 2018](#), and discussion therein). FIRE-2 includes the same stellar feedback channels as EMP-*Pathfinder*, namely supernovae Type II and Ia and stellar winds from AGB stars. However, in addition FIRE-2 also includes early stellar feedback from young massive stars, in the form of stellar winds, photoionization, photoelectric heating and radiation pressure from OB stars. Haloes were identified at $z = 0$ using the AMIGA halo finder ([Gill et al. 2004](#); [Knollmann & Knebe 2009](#)).

2.3 The sample

Table 1 summarises the basic properties of the different simulation sub-sets. The initial conditions for the EMP-*Pathfinder* galaxies were selected to have halo masses in the range $11.85 \leq \log(M_{\text{halo}}/M_{\odot}) \leq 12.3$ at $z = 0$, comparable to that of the Milky Way (e.g. [Bland-Hawthorn & Gerhard 2016](#)). We thus apply the same halo mass cut to select the FIREBOX galaxies for this analysis. The full sample comprises 21 *Pathfinder*-cSFE, 14 *Pathfinder*-mffSFE and 26 FIREBOX central galaxies. However, some of these galaxies are visually classified as undergoing a major merger or interaction at $z = 0$, hence we exclude them from the analysis. The reduced sample consists of 14 *Pathfinder*-cSFE, 12 *Pathfinder*-mffSFE and 20 FIREBOX galaxies.

2.3.1 Calculating f_{HI}

Although all simulations track ‘HI’, EMP-*Pathfinder* via the Grackle non-equilibrium chemistry network and FIREBOX based on CLOUDY tables that include the contributions from the UV-Background and local radiation from stars (see [Hopkins et al. 2014, 2018](#), for details), this encompasses the entire neutral hydrogen phase, i.e. HI and H₂. None of the simulations include non-equilibrium chemistry for H₂. Thus, we use two empirically-motivated models, one for each simulation, to estimate the molecular fraction of the gas and then subtract it from the total neutral gas fraction, to obtain the ‘true’ HI fraction of each gas particle.

³ <https://fire.northwestern.edu/>

⁴ <http://www.tapir.caltech.edu/~phopkins/Site/GIZMO.html>

We use the empirical [Blitz & Rosolowsky \(2006\)](#) scaling relation between the gas pressure and H_2 to HI ratio to determine M_{HI} for the EMP-*Pathfinder* galaxies. Specifically, they found that

$$R_{\text{mol}} \equiv \frac{\Sigma_{\text{H}_2}}{\Sigma_{\text{HI}}} = \left(\frac{P}{P_0} \right)^\alpha, \quad (3)$$

where P is the mid-plane pressure of the gas, and P_0 and α are free parameters, calibrated from the observations of nearby galaxies. Following [Marinacci et al. \(2017\)](#), we use the [Leroy et al. \(2008\)](#) values of $P_0 = 1.7 \times 10^4 \text{ K cm}^{-3}$ and $\alpha = 0.8$. The molecular fraction of neutral gas $f_{\text{H}_2, \text{neutral}}$ is then given by $R_{\text{mol}} / (R_{\text{mol}} + 1)$ and the HI mass of each gas particle can be calculated as $M_{\text{HI}, i} = f_{\text{neutral}, i} \times (1 - f_{\text{H}_2, \text{neutral}, i}) \times M_i$ from the particle mass M_i , the neutral hydrogen fraction $f_{\text{neutral}, i}$ and the pressure P_i .

While not including non-equilibrium chemistry, the FIRE-2 model uses Equation 1 of [Krumholz & Gnedin \(2011\)](#) to estimate $f_{\text{H}_2, \text{neutral}}$ at run-time. This is an analytical model calibrated with high-resolution radiative transfer, non-equilibrium H_2 chemistry simulations of an idealised spherical cloud embedded in a Lyman-Werner background. In the [Krumholz & Gnedin \(2011\)](#) model, $f_{\text{H}_2, \text{neutral}}$ depends on the dust optical depth and the metallicity of the cloud. The dust optical depth scales with the surface density of the gas, which is calculated from the volume density and the scale height (obtained via a Sobolev approximation on the density).

We use two different models to estimate $f_{\text{H}_2, \text{neutral}}$ for the EMP-*Pathfinder* and FIREbox galaxies on account of the differences in the simulation setup. While the pressure-based [Blitz & Rosolowsky \(2006\)](#) estimate is more empirically motivated, FIREbox was calibrated using the [Krumholz & Gnedin \(2011\)](#) model. Using the pressure-based approach for FIREbox leads to lower $f_{\text{H}_2, \text{neutral}}$ and thus higher HI masses and surface densities for the FIREbox galaxies (Σ_{HI} of $20\text{--}30 \text{ M}_\odot \text{ pc}^{-2}$ in the central regions of all galaxies cf. $\approx 10 \text{ M}_\odot \text{ pc}^{-2}$ with the [Krumholz & Gnedin \(2011\)](#) model). Conversely, using the [Krumholz & Gnedin \(2011\)](#) model leads to lower $f_{\text{H}_2, \text{neutral}}$ and higher HI fractions for the EMP-*Pathfinder* galaxies, in particular for *Pathfinder*-mffSFE, compared to the pressure-based recipe (also yielding Σ_{HI} of $20\text{--}30 \text{ M}_\odot \text{ pc}^{-2}$ in the central regions of half the galaxies in the sample). This likely results from the coarser spatial resolution in the EMP-*Pathfinder* simulation compared to FIREbox (minimum gas gravitational softening of 83.6 pc at $z = 0$ compared to 4.2 pc respectively, see Table 1). The optical depth estimates obtained for the high-density, high-pressure regions, which are especially prominent in the centres of *Pathfinder*-mffSFE galaxies, are likely underestimates, thus leading to an underestimation of $f_{\text{H}_2, \text{neutral}}$. Since observations suggest that $\sim 10 \text{ M}_\odot \text{ pc}^{-2}$ (e.g. [Blitz & Rosolowsky 2006](#); [Bigiel et al. 2008](#)) is a threshold above which gas tends to be molecular, we selected the model that best reproduces this behaviour for the simulated galaxies as the fiducial way to calculate the HI fraction of the galaxies. The qualitative results of this paper remain the same, independent of which model is used; however, there are some quantitative differences, which we discuss in Appendix A.

The resultant HI distributions in EMP-*Pathfinder* and FIREbox are in good agreement, despite the different chemistry/cooling treatment and ways to calculate f_{HI} . The distribution in temperature is bimodal, with the majority of HI in the warm phase ($T > 5000 \text{ K}$).

2.3.2 The HI main sequence

Figure 1 shows the HI-to-stellar mass ratio of the galaxies as a function of their stellar mass, colour-coded by their star formation rate.

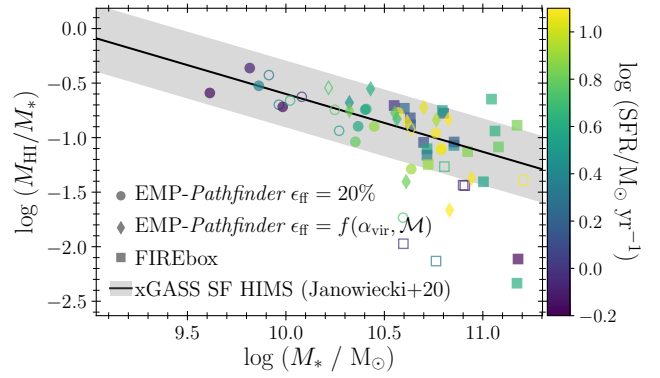


Figure 1. HI-to-stellar mass fraction as a function of stellar mass of the simulated galaxies in our sample. The data are colour-coded by their star formation rate, with different symbols denoting the different sub-grid physics samples. Empty symbols denote the galaxies excluded from further analysis, due to interactions. The data are overplotted on the HI main sequence relation of the star-forming xGASS ([Catinella et al. 2018](#)) galaxies from [Janowiecki et al. \(2020\)](#) shown as a solid black line, and the 0.3 dex uncertainty in grey shading.

Filled symbols denote the galaxies considered for the analysis presented in the remainder of this paper, while the open symbols show the galaxies that are excluded due to interactions. The simulation data are overplotted on the xGASS ([Catinella et al. 2018](#)) HI ‘main sequence’ of star-forming galaxies ([Janowiecki et al. 2020](#)) shown as a black line with the 0.3 dex scatter around this HI main sequence relation indicated through grey shading. Despite their similar halo masses at $z = 0$, the galaxies evolved with the different sub-grid physics models are clustered in different parts of in the HI -to-stellar mass fraction - stellar mass plane, highlighting the impact of subtle differences in baryonic physics on galaxy evolution across cosmic time. While there is overlap between all simulation sub-sets around the stellar mass of the Milky Way $\log(M_*/M_\odot) \sim 10.7$ (e.g. [Cautun et al. 2020](#)), the *Pathfinder*-cSFE galaxies tend to be undermassive (10 galaxies with $\log(M_*/M_\odot) \leq 10.3$) and the FIREbox galaxies extend to higher stellar masses (8 galaxies with $\log(M_*/M_\odot) \geq 11$). The HI -to-stellar mass fractions of all simulated galaxy sub-sets are in good agreement with the observations, scattering around the HI main sequence mostly within the ± 0.3 dex scatter.

3 HI DISC PROPERTIES

In this section, we examine the properties of the HI discs in more detail, beginning with properties that have been observationally well-established. To do so, we rotate all galaxies such that the HI disc is face-on, i.e. in the x - y plane and the angular momentum vector of the gas, calculated based on all gas within the central 5 kpc, is perpendicular to it. Specifically, we examine the HI mass-size relation (Section 3.1), radial HI surface density and scale height profiles (Sections 3.2 and Sections 3.3, respectively).

3.1 HI mass-size relation

The HI mass-size relation relates the mass of HI enclosed within the HI scale radius (R_{HI} , the radius of the HI disc where $\Sigma_{\text{HI}} = 1 \text{ M}_\odot \text{ pc}^{-2}$) to the diameter of the HI disc ($D_{\text{HI}} = 2 R_{\text{HI}}$). It is a very tight relation that has a slope of ~ 0.5 , and has been well established empirically (e.g. [Broeils & Rhee 1997](#); [Swaters et al. 2002](#); [Begum](#)

Table 1. Properties of the simulation sub-samples.

| Name | N_{gal} | m_{b} ($10^4 M_{\odot}$) | m_{DM} ($10^5 M_{\odot}$) | $\epsilon_{\text{gas}}^{\text{min}}$ (pc) | $d_{\text{HI}}^{\text{med}}$ (pc) | ϵ_{stars} (pc) | ϵ_{DM} (pc) | n_{th} (cm^{-3}) | other SF criteria | ϵ_{ff} | e_{SN} (ergs) |
|--|------------------|--|---|--|--------------------------------------|-----------------------------------|--------------------------------|---|--|---------------------------------------|---------------------------|
| EMP-Pathfinder $\epsilon_{\text{ff}} = 20\%$ | 21 / 14 | 22.6 | 14.4 | 83.6 | 145 | 175 | 320 | 1 | $T < 1.5 \times 10^4 \text{ K}$ | 0.2 | 3×10^{51} |
| EMP-Pathfinder $\epsilon_{\text{ff}} = f(\alpha_{\text{vir}}, \mathcal{M})$ | 14 / 12 | 22.6 | 14.4 | 83.6 | 120 | 175 | 320 | 1 | $T < 1.5 \times 10^4 \text{ K}$ | $f(\alpha_{\text{vir}}, \mathcal{M})$ | 3×10^{51} |
| FIREBOX | 26 / 20 | 6.26 | 3.35 | 4.2 | 76 | 12 | 80 | 300 | $\alpha_{\text{vir}} < 1, f_{\text{H}_2}, M_{\text{J}} < m_{\text{b}}$ | 1 | 10^{51} |

Notes: For each baryonic physics sub-sample, column 1 lists the name of the sub-sample, column 2 lists the total / non-interacting number of galaxies in the sample, column 3 lists the baryonic mass resolution, column 4 the dark matter mass resolution, columns 5 lists the minimum gravitational softening for gas, column 6 lists the HI mass-weighted median inter-particle spacing in the central regions of the galaxies, columns 7 and 8 list the Plummer-equivalent gravitational softening for stars and dark matter (all at $z = 0$), column 9 lists the density threshold for star formation, column 10 lists other star formation criteria, column 11 lists the star formation efficiency per free-fall time and column 12 lists the energy injected per supernova.

et al. 2008; Lelli et al. 2016; Wang et al. 2016; Stevens et al. 2019; Rajohnson et al. 2022). It can serve as a test for the (baryonic physics) of cosmological simulations: due to the robustness of the HI mass-size relation, simulated galaxies should lie on the relation, unless the star formation and/or stellar feedback physics result in very disturbed HI disc morphologies containing enormous ‘holes’ (Stevens et al. 2019, see also the EAGLE HI mass-size relation and the discussion regarding unphysically large HI holes in Bahé et al. 2016).

The main panel of Figure 2 shows the HI mass-size relation for our sample of simulated galaxies, with histograms showing the marginal distributions of M_{HI} and D_{HI} . Grey crosses show the data for MIGHTEE spirals, and the dashed line shows the most recent empirical fit for the HI mass-size relation to this data (Rajohnson et al. 2022). To first order, all galaxy sub-sets lie on the HI mass-size relation, with a scatter comparable to that of the observations. The *Pathfinder*-mffSFE galaxies are in excellent agreement with the MIGHTEE fit. The *Pathfinder*-cSFE galaxies tend to have slightly under-massive HI discs for their sizes, the opposite holds for FIREBOX galaxies, which tend to be a little over-massive at a fixed D_{HI} , compared to the MIGHTEE fit.

3.2 HI surface density profiles

Next, we turn to the radial HI surface density profiles, which we compute in rolling bins of width 1 kpc. In the outskirts of the HI disc ($R/R_{\text{HI}} \geq 0.8$), the Σ_{HI} profiles of observed late-type and low-mass galaxies decline exponentially (e.g. Swaters et al. 2002; Obreschkow et al. 2009; Bigiel & Blitz 2012; Wang et al. 2014). The shape and normalisation of the inner profile tend to vary between galaxies, observational samples and morphological types, with central median Σ_{HI} ranging from 4 to $8 M_{\odot} \text{pc}^{-2}$ for dwarfs and late-type galaxies with stellar masses to $10^{11} M_{\odot}$ (Wang et al. 2016, in particular their Figure 2 for a compilation of median profiles from observational surveys, and references therein).

Figure 3 shows the median radial HI surface density profiles of our galaxy sub-sets, the shaded regions indicating the error on the median determined via bootstrapping, with the Wang et al. (2014) exponential trend of the outer Σ_{HI} profile overplotted as a grey-dashed line and the range of median central HI surface densities of the observational compilation in Wang et al. (2016) indicated by a grey box. All median profiles follow the exponential profile in the outskirts of the disc (*Pathfinder*-mffSFE and FIREBOX for $R \geq 0.8R_{\text{HI}}$, *Pathfinder*-cSFE only for $R \geq R_{\text{HI}}$), however, the inner profiles differ both in shape and normalisation. *Pathfinder*-cSFE has a centrally peaked median HI profile ($5 M_{\odot} \text{pc}^{-2}$), which declines by $\sim 4 M_{\odot} \text{pc}^{-2}$ before

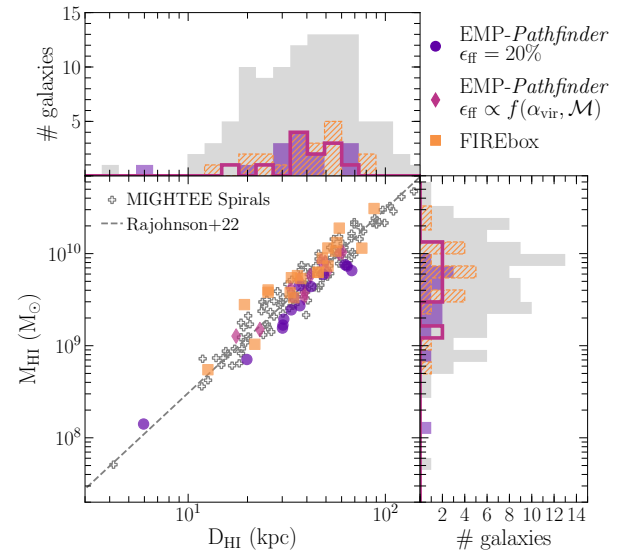


Figure 2. HI mass-size relation for the galaxies in our sample. Purple circles denote the *Pathfinder*-cSFE galaxies, magenta diamonds denote the *Pathfinder*-mffSFE galaxies, and orange squares denote the FIREBOX galaxies. Histograms show the marginal distributions for each indicator and galaxy sub-set. The grey crosses show the observational data from MIGHTEE, the grey dashed line shows their best-fit HI mass-size relation (Rajohnson et al. 2022). All simulated galaxies scatter tightly around the observed HI mass-size relation.

dropping off exponentially. By contrast, the *Pathfinder*-mffSFE profile is approximately constant at $\sim 5 M_{\odot} \text{pc}^{-2}$ as a function of radius, before declining exponentially at $R > 0.8R_{\text{HI}}$. The median FIREBOX Σ_{HI} profile is approximately constant at $8 M_{\odot} \text{pc}^{-2}$ to $R = 0.3R_{\text{HI}}$, before gradually declining to $5 M_{\odot} \text{pc}^{-2}$ at $R = 0.8R_{\text{HI}}$ and declining exponentially at larger radii. The central profiles of all simulated galaxy sub-sets fall within the profile shapes and magnitudes found within galaxies in the local Universe.

3.3 HI scale heights

Following Gensior et al. (2023b), we compute the HI scale height of the simulated galaxies in radial annuli of 1 kpc width, in the 4 kpc surrounding the galactic mid-plane. The vertical, volumetric gas

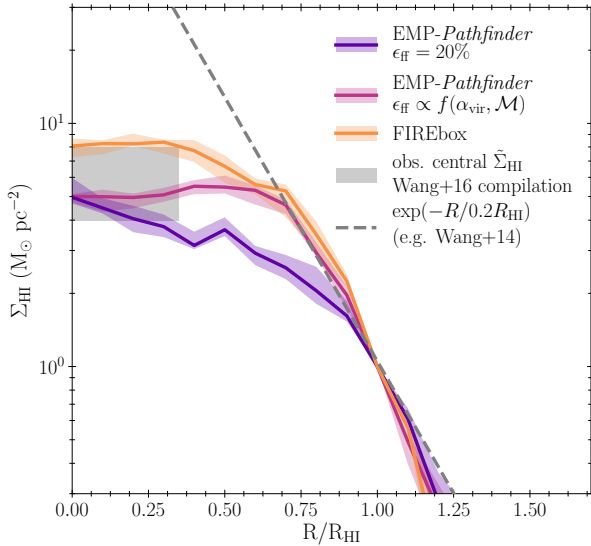


Figure 3. HI gas surface density profiles as a function of galactocentric radius scaled by the HI scale radius R_{HI} (defined as radius where $\Sigma_{\text{HI}} = 1 \text{ M}_{\odot} \text{pc}^{-2}$). Coloured lines and shaded regions denote the median and the error on the median, determined via bootstrapping, of each different baryonic physics sub-sample, respectively, with the Wang et al. (2014) exponential fit to the outer regions of observed HI surface density profiles overplotted as a grey-dashed line. For comparison, the grey shaded box indicates the central range of the median Σ_{HI} from 8 different observational samples, compiled by Wang et al. (2016). While all simulated galaxy sub-sets approximately follow the exponential profile at $R \geq 0.8R_{\text{HI}}$, the central HI mass surface density differs in both shape and normalisation.

density distribution in each annulus is fit with a Gaussian profile, $\rho(z) \propto \exp(-z^2/(2h_{\text{HI}}^2))$, which depends on the HI scale height, h_{HI} . Figure 4 shows the median radial HI scale height profiles for the different sub-grid physics sub-sets, with the Bacchini et al. (2019) scale heights for 12 THINGS galaxies, computed by iteratively fitting the vertical volume density profile (estimated from the total gravitational potential) with a Gaussian, overplotted.

All simulated HI discs increase in thickness from a median of $\sim 100 \text{ pc}$ (*Pathfinder*-mffSFE and FIREbox) – 200 pc (*Pathfinder*-cSFE) in the centre to $\sim 1 \text{ kpc}$ in the outskirts of the disc, i.e. exhibit flaring. In contrast to the other two simulated galaxy sub-sets, the median scale height of the *Pathfinder*-cSFE galaxies increases steeply from $\sim 200 \text{ pc}$ to $\sim 700 \text{ pc}$ within the central 3 kpc, before rising more shallowly to 1 kpc at larger radii. The median h_{HI} of the *Pathfinder*-mffSFE galaxies also increases moderately from $\sim 100 \text{ pc}$ to $\sim 300 \text{ pc}$ within the central 3 kpc before increasing more gradually, compared to the FIREbox galaxies’ h_{HI} , which increases gradually throughout the disc. The median HI scale heights of both *Pathfinder*-mffSFE and FIREbox galaxies are in good agreement with the THINGS observations within the inner 10 – 15 kpc, with only the FIREbox galaxies matching the observations with scale heights of several hundred pc in the outskirts of the HI discs. The discs of the *Pathfinder*-cSFE galaxies are consistently thicker than those of the other sub-sets of simulated galaxies and observations (compared to both THINGS (Bacchini et al. 2019; Patra 2020), but also the BLUEDISK galaxies (Randriamampandry et al. 2021), which have similar scale heights).

High resolution has been important for reproducing thin discs in simulations (e.g. Guedes et al. 2011, Pillepich et al. 2019, see also

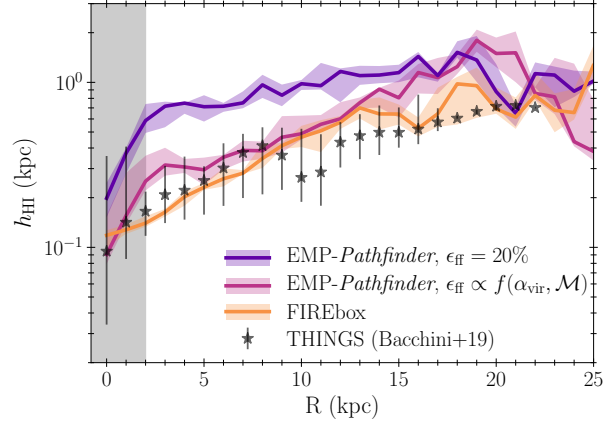


Figure 4. Radial profiles of the HI disc scale heights of the simulated galaxies, measured by fitting a Gaussian to the vertical volume density distribution in kpc bins. Coloured lines and shaded regions denote the median and the error on the median, determined via bootstrapping, of each different baryonic physics subsample, respectively, with the THINGS scale heights (Bacchini et al. 2019) overplotted as black stars. The grey shaded region indicates the central region where scale heights are marginally resolved. The *Pathfinder*-cSFE HI discs are substantially thicker than those observed in the nearby universe within the inner $\sim 10 \text{ kpc}$.

discussion in Gensior et al. 2023b). FIREbox has a minimum gravitational softening of 4.2 pc for the gas and a Plummer-equivalent softening of 12 pc for the stars, which suggests that gravity around the mid-plane is well resolved in both the gaseous and stellar component. The minimum gravitational softening length for gas in *EMP-Pathfinder* is 83.6 pc (and the approximate gas cell radius will be a factor of ~ 3 smaller per definition), while the Plummer-equivalent softening of the stars is 175 pc. Thus, the stellar density near the mid-plane might be underestimated. However, the median HI scale height of *Pathfinder*-cSFE galaxies enters the spatial regime where stellar gravity is well resolved ($h_{\text{HI}} > \epsilon_*$) for $R > 1.5 \text{ kpc}$, while significant differences to the (much) lower median *Pathfinder*-mffSFE h_{HI} , which is broadly consistent with both FIREbox and the observations, persist out to $R = 15 \text{ kpc}$. Since the densest gas is likely predominantly molecular, the HI mass-weighted median inter-particle spacing, $d_1 = (m_1/\rho_1)^{1/3}$, calculated from the mass and density of each particle, can give a better idea of the characteristic size of HI-dominated particles. The inter-particle spacing in the central region is listed in column 6 of Table 1 and is 76 pc for FIREbox, 120 pc for *Pathfinder*-mffSFE and 145 pc for *Pathfinder*-cSFE, respectively. This indicates that the scale heights in the central 1–2 kpc are marginally resolved, shown as the grey-shaded region in Figure 4, while h_{HI} will be resolved by several cells at larger galactocentric radii. Therefore, this implies that the underlying physics is the driver of the HI scale height trends, and that the (*EMP-Pathfinder*) resolution adequately resolves the scale heights for $R \geq 2 \text{ kpc}$.

Analysing (different ways to calculate the) HI scale heights in FIREbox galaxies, Gensior et al. (2023b) concluded that self-consistently modelling a multi-phase ISM that includes a cold phase could be a reason that the FIREbox galaxies have thin HI discs, in good agreement with observations. Comparing the observational results (and FIREbox) to those of the *EMP-Pathfinder* galaxies, in particular to the *Pathfinder*-cSFE galaxies which have discs that are consistently too thick, highlights that including a cold ISM is not a sufficient criterion for producing the thin HI discs. Figure 4 suggests

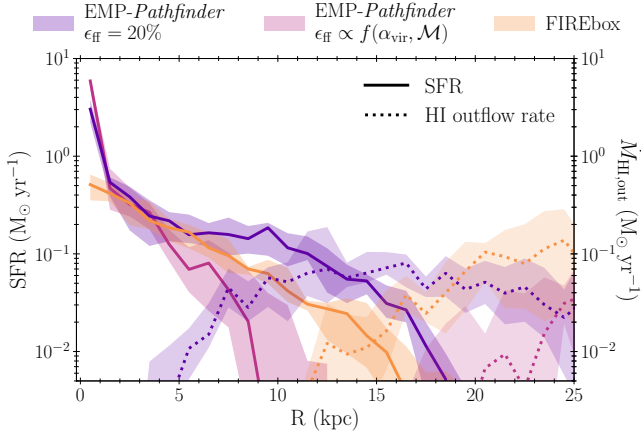


Figure 5. Radial profiles of the median star formation rates (averaged over a period of 100 Myr, solid lines) and HI outflow rates (HI mass moving away from the galactic midplane in a 500 pc wide slab 5 kpc above and below the midplane, dotted lines) for the different simulated galaxy sub-sets. Coloured lines and shaded regions denote the median and the error on the median of each property, determined via bootstrapping, respectively.

that more empirically motivated sub-grid physics are required, either in the form of an environmentally-dependent SFE or early stellar feedback (which for the EMP family of simulations will be presented by Keller et al. in prep.; Kruijssen et al. in prep.). Both result in changes in location and strength of the stellar feedback compared to the *Pathfinder*-cSFE case, reflected in the differences in the global galaxy, gas and star formation properties after an evolution across cosmic time.

We show the median radial profiles of the SFR, averaged over the past 100 Myr, and the HI outflow rates, calculated as the mass moving away from the galaxy in a 500 pc wide slice located 5 kpc above and below the midplane, in Figure 5. The median SFR is much more centrally peaked in the *EMP-Pathfinder* galaxies compared to *FIREbox*, which through the resultant stellar feedback likely leads to the steeper increase in h_{HI} of *EMP-Pathfinder* galaxies within the inner 3 kpc. Additionally, the *Pathfinder*-cSFE galaxies experience much stronger outflows in the central 15 kpc, compared to *Pathfinder*-mffSFE and *FIREbox* galaxies, suggesting that the *Pathfinder*-cSFE HI discs are puffed up by feedback. This is in agreement with the results [Benítez-Llambay et al. \(2018\)](#), who found that the gas discs in *EAGLE* were too thick due to the strong stellar feedback.

4 HI DISC MORPHOLOGIES

We quantify the structure of the HI discs using the non-parametric morphological indicators. These indicators are most commonly used to classify galaxy stellar morphologies in the optical (e.g. [Abraham et al. 1994, 1996](#); [Conselice 2003](#); [Lotz et al. 2004](#); [Rodríguez-Gomez et al. 2019](#)). However, they have also been used to study the morphology of HI discs, particularly trying to identify mergers and interactions (e.g. [Holwerda et al. 2011a,b](#)), ram pressure stripping (e.g. [Holwerda et al. 2023](#)) and to assess how well property-matched *IllustrisTNG50* galaxies resemble *WHISP* galaxies ([Gebek et al. 2023](#)). Furthermore, [Davis et al. \(2022\)](#) used the Gini, Asymmetry and Smoothness indicators to quantify the molecular gas morphologies in the central 3 kpc of a sample of late- and early-type galaxies from the mm-Wave Interferometric Survey of Dark Object Masses (*WISDOM*) project and *Physics at High Angular Resolu-*

tion in Nearby Galaxies (*PHANGS*; [Leroy et al. 2021](#)) survey and correlate the central ISM morphologies with galaxy properties.

4.1 Method

Here we focus on the Asymmetry, Smoothness and Gini indicators to quantify the structure of the entire HI disc of the galaxies. We utilise the ray-tracing capability of *AREPO* to generate HI surface density projections for every simulated galaxy in the sample, including those from *FIREbox*. Since the majority of HI is in the warm phase, surface density maps should provide a reasonable estimate of the HI emission, but a full forward modelling with radiative transfer would be desirable for an one-to-one comparison with observations. The projections are generated face-on, in a box 60 kpc a side, centred on the centre of the galaxy. This is defined as the position of the particle with the minimum gravitational potential energy for *EMP-Pathfinder* haloes identified with *SUBFIND* and corresponds to the position where the total matter density is maximised for *FIREbox* haloes identified with *AMIGA*. The HI surface density maps have an intrinsic resolution of 20 pc per pixel. We then apply a Gaussian smoothing kernel with full-width half-maximum corresponding to 80 pc, comparable to the minimum gravitational softening length of the *EMP-Pathfinder* galaxies. Prior to computing the nonparametric morphological indicators, we apply a surface density cut corresponding to a HI column density of $7 \times 10^{19} \text{ cm}^{-2}$, comparable in sensitivity to e.g. the *BLUEDISK* ([Wang et al. 2013](#)) or *THINGS* ([Walter et al. 2008](#)) data and well within the sensitivity of *SKA*-precursor surveys *MHONGOOSE* ([de Blok et al. 2016](#)) and *MIGHTEE* ([Maddox et al. 2021](#)).

As a test for these choices, we also explore how a more conservative cut affects the results by recomputing the statistics for a cut at $3 \times 10^{20} \text{ cm}^{-2}$, and at a coarser resolution of 500 pc. Furthermore, we also create maps at inclinations of 10, 30, 50 and 70° and measure Gini, Smoothness and Asymmetry. Notably, the qualitative trends discussed in Section 4.2 are not strongly affected by these changes, as especially the Asymmetry varies little with inclination. We refer the reader to Appendix B for a more extensive discussion.

We follow [Davis et al. \(2022\)](#) and calculate the Asymmetry, A , as:

$$A \equiv \frac{\sum_{i,j} |I_{ij} - I_{ij}^{180}|}{\sum_{i,j} |I_{ij}|}, \quad (4)$$

where I_{ij} is the surface density of the pixel in position ij , and I_{ij}^{180} the surface density of the pixel in the same position after the map has been rotated by 180 degrees, and the total Asymmetry⁵ is obtained by summing over all pixel positions i, j in the map. A lower value of A corresponds to a more rotationally symmetric gas distribution, where $A = 0$ indicates perfect rotational symmetry and $A = 2$ complete asymmetry with all flux concentrated in one half of the map.

The Smoothness, S , is defined as:

$$S \equiv \frac{\sum_{i,j} |I_{ij} - I_{ij}^S|}{\sum_{i,j} I_{ij}}, \quad (5)$$

where I_{ij}^S is the surface density of the pixel ij after it has been

⁵ Using different definitions of A , such as replacing the denominator of Equation 4.1 by $\sum_{i,j} |I_{ij} + I_{ij}^{180}|$ (e.g. [Lelli et al. 2014](#)), or squaring the difference instead of using absolutes (e.g. [Deg et al. 2023](#)), affects the value of A , but has no impact on the results presented in this paper.

smoothed with a boxcar filter of width σ . In optical studies, the width of the boxcar filter is commonly set to 0.25 Petrosian radii and thus varies for each galaxy (e.g. [Rodríguez-Gomez et al. 2019](#)), while [Davis et al. \(2022\)](#) use the same smoothing filter width for all galaxies. Following [Davis et al. \(2022\)](#), we also use a single σ , i.e. fix the width of the boxcar filter for all galaxies. Specifically, we choose $\sigma = 4$ kpc, which is still significantly larger than the 500 pc resolution of the coarser maps and comparable to a quarter of the Petrosian radius expected for discs this size. Furthermore, we have verified that varying the boxcar filter width only affects the absolute value of S measured (larger smoothing kernel widths leading to higher values of S), but not the trends seen between the different physics sub-sets, in agreement with [Davis et al. \(2022\)](#) findings. Similar to the Asymmetry coefficient, a lower value of S corresponds to a smoother gas distribution.

The Gini coefficient, G , is calculated as:

$$G \equiv \frac{1}{\bar{X}n(n-1)} \sum_{i=1}^n (2i - n - 1)X_i, \quad (6)$$

where \bar{X} is the mean surface density measured over all pixels $i = 1, 2, \dots, n$ and X_i the surface density of each individual pixel. The Gini coefficient measures how homogeneously the flux is distributed across the map, where a completely homogeneous brightness distribution yields $G = 0$ and $G = 1$ corresponds to all flux being concentrated in a single pixel.

4.2 Results

The main panels of Figure 6 show the Smoothness, Gini and Asymmetry coefficients for the different simulated galaxy sub-sets, plotted against each other, while their marginal distributions are shown as histograms on the side. There is a strong correlation between Smoothness and Asymmetry for all individual sub-sets of galaxies simulated with different sub-grid physics and for the entire sample. No statistically significant correlation is present between Gini and Smoothness or Gini and Asymmetry for either the different simulated galaxy sub-sets or the entire sample.

Remarkably, the different physics sub-sets occupy different parts of the parameter space in Smoothness and Asymmetry, demonstrating that the non-parametric HI morphology is a sensitive test of sub-grid physics in simulations. The *Pathfinder*-mffSFE galaxies are the smoothest and most symmetric (6 galaxies with $S < 0.15$ and $A < 0.6$), whilst the *Pathfinder*-cSFE galaxies are the least smooth and most asymmetric (12 galaxies with $A > 1$). FIREBOX galaxies occupy the intermediate parameter space between the EMP-*Pathfinder* galaxies, although there is significant overlap in the Smoothness of FIREBOX and *Pathfinder*-cSFE galaxies ($0.2 \leq S \leq 0.3$).

All galaxies have $G \geq 0.6$, with a large scatter. The high Gini values are likely a consequence of the HI surface density distribution in these objects. Especially in the *Pathfinder*-mffSFE and FIREBOX case, the surface density profiles are roughly constant until they decline exponentially (see Figure 3), but even for *Pathfinder*-cSFE there is a sharp contrast between the higher density regions in the HI disc as the density rapidly drops below the density threshold. As Gini measures the inequality in the density distribution, it is therefore not surprising that it is more similar between the different physics sub-sets and is less sensitive to the disc morphology than Smoothness and Asymmetry.

None the less, Figure 6 (and Figures B1 – B4) highlight the impact of the different baryonic sub-grid physics on the distribution of HI within the gas discs. We show some example surface

density projections in Figure 7. The *Pathfinder*-cSFE galaxies are characterised by large ‘holes’⁶ within the HI disc. These large holes, combined with asymmetrically distributed bright clumps of HI result in the large Asymmetry and Smoothness values for the *Pathfinder*-cSFE galaxies. FIREBOX galaxies are the most similar between them: all HI distributions look similar to a flocculent spiral, with small holes as the result of stellar feedback. The *Pathfinder*-mffSFE sample is split between galaxies with similar morphologies to those of FIREBOX and the very smooth, fairly uniform density and hole-free galaxies that occupy the bottom left corner of the Smoothness-Asymmetry parameter space. Both FIREBOX and *Pathfinder*-cSFE allow star formation anywhere within the disc (wherever the density threshold is met, which for FIRE usually means that the other eligibility criteria are also met, see [Hopkins et al. 2018](#)). The only stellar feedback channel in EMP-*Pathfinder* galaxies is the SN feedback, leading to huge bubbles in the *Pathfinder*-cSFE galaxies. The early stellar feedback in FIREBOX likely pre-processes the ISM in the natal environment of the stars, making it easier for the SN feedback to escape vertically rather than expanding into the plane of the galaxy, thus leading to smaller holes (which is qualitatively similar to the behaviour of EMP-*Pathfinder* combined with early stellar feedback in isolated galaxies, see Figure 8 in [Keller et al. 2022](#)). Contrary to that, the turbulence-based star formation model in *Pathfinder*-mffSFE places much stronger restrictions on the conditions where stars may form, with more centrally concentrated star formation, thus leading to (a sub-set of) much smoother, more symmetric HI discs.

While non-parametric morphological indicators have been measured for (some) THINGS and WHISP galaxies, a direct comparison between observations and our simulations is not straightforward. The absolute values of the non-parametric indicators depend sensitively on the maps from which they are calculated (and can be biased by the observational S/N and point-spread function of the beam, [Thorp et al. 2021](#)). Thus a comparison between HI mock observations of the simulations and observations, measuring the non-parametric morphological indicators in exactly the same way would be desirable. We defer this to future work.

5 ASYMMETRY AS TRACER OF THE BARYONIC PHYSICS

We perform a random forest regression (RFR), using `scikit-learn` ([Pedregosa et al. 2011](#)), to gain a better intuition about the drivers behind the different HI morphologies across the simulated galaxies. The random forest model is trained to predict each non-parametric morphological indicator based on a number of global and local galaxy properties. It returns a list of feature importances, i.e. how important each respective property is for the model to predict Gini, Smoothness or Asymmetry. RFR is one of the most powerful and simple non-linear regression methods, particularly suited to assess feature importances for large astronomical datasets ([Donalek et al. 2013](#)). Hence, we turn to RFRs to infer which features are the most important to predict the non-parametric morphological indicators, because there are a large number of plausible potential drivers, many of which show some level of (anti-)correlation with the non-parametric morphological indicators. Specifically, we consider the global parameters galaxy stellar mass, M_* , central stellar surface density, μ_* , the stellar velocity dispersion in the central kpc $\sigma_{*,\text{central}}$, and the radius of

⁶ Rather than being completely devoid of HI the gas is at densities lower than our respective column density threshold.

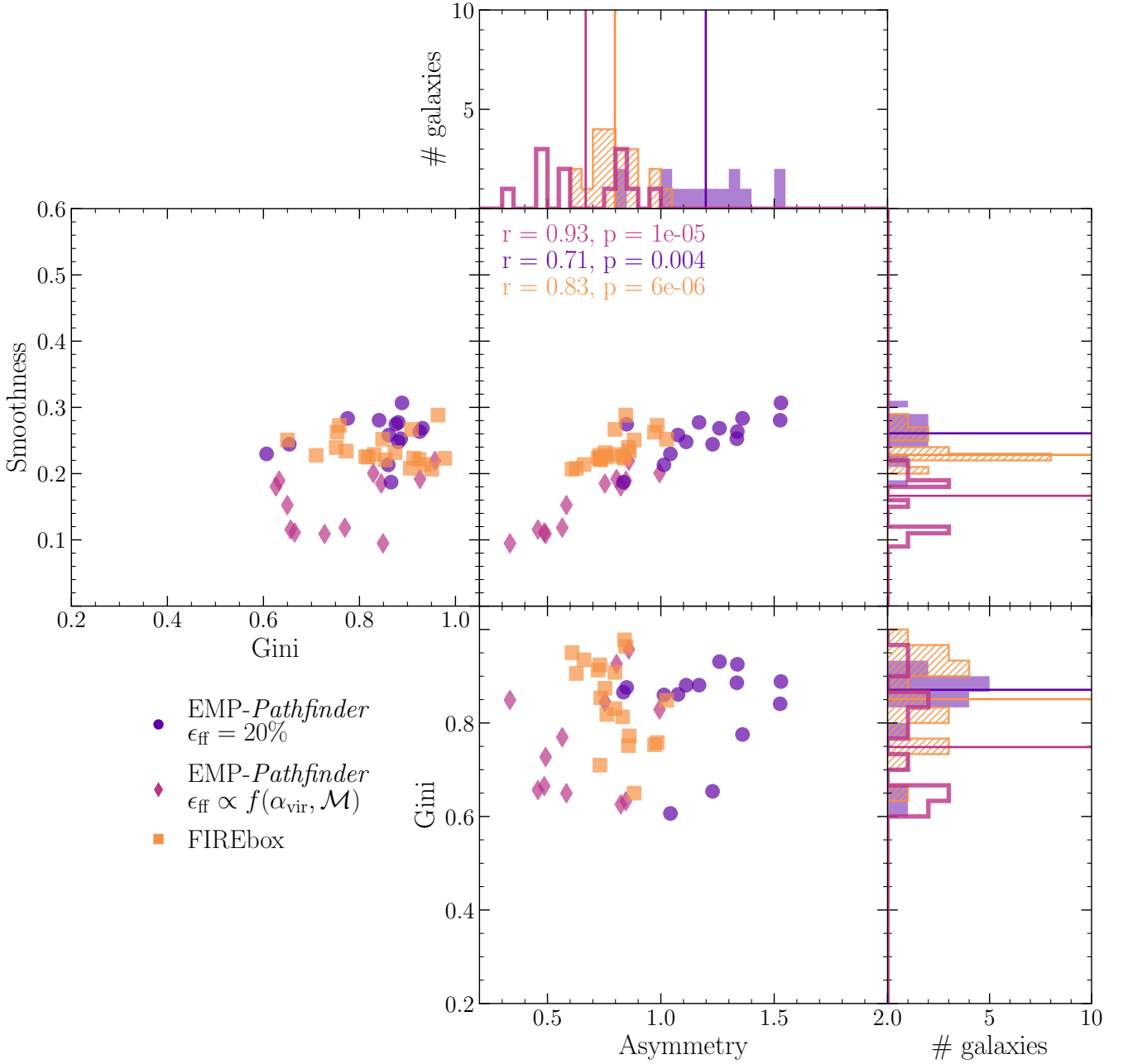


Figure 6. HI morphology as classified by the non-parametric morphological indicators Smoothness, Gini and Asymmetry (plotted against each other in the three main panels) measured from face-on HI surface density projections of the galaxies with a resolution of 80 pc and column density threshold of $7 \times 10^{19} \text{ cm}^{-2}$. Purple circles denote the *Pathfinder*-cSFE galaxies, while magenta diamonds denote the *Pathfinder*-mffSFE galaxies, and orange squares denote the FIREbox galaxies. Histograms show the marginal distributions for each indicator and galaxy sub-set, the median values are indicated by coloured lines. A statistically significant correlation between Smoothness and Asymmetry is present for each simulated galaxy sub-sets, the Spearman rank correlation coefficient and p -value are indicated in the top left corner of the panel in the respective colour of each sub-set. No statistically significant correlations are present between Gini and Smoothness or Asymmetry. The galaxies simulated with different sub-grid physics occupy distinctly different parts of the Asymmetry-Smoothness parameter space.

the galaxy $R_{\text{gal}} (= 0.1R_{\text{halo}})$; the HI and gas properties such as the HI mass enclosed in the HI scale radius, $M_{\text{HI}}(R < R_{\text{HI}})$, the HI scale radius R_{HI} , the HI mass enclosed within the galaxy $M_{\text{HI}}(R < R_{\text{gal}})$, the total gas mass enclosed within the galaxy $M_{\text{gas}}(R < R_{\text{gal}})$, the average HI and total gas surface densities within the central kpc, R_{HI} and the galaxy, $\Sigma_{\text{HI}}(R < 1 \text{ kpc})$, Σ_{gas} , $\Sigma_{\text{HI}}(R < R_{\text{HI}})$, f_{HI} , (f_{gas}) respectively; the SFR, specific SFR (sSFR = SFR/M_*), HI SFE

(=SFR/ M_{HI}) and star-forming main sequence offset (with respect to the [Catinella et al. 2018](#) xGASS main sequence) for 10 and 100 Myr averaging timescales and outflow rates for the total gas, $\dot{M}_{\text{gas, out}}$, and the HI, $\dot{M}_{\text{HI, out}}$, calculated, as in Section 3.3, as the mass flux away from the midplane in a 500 pc thick slab, 5 kpc above and below the galactic midplane. For all physical quantities listed, a single value per galaxy is used. In addition to performing the random forest regres-

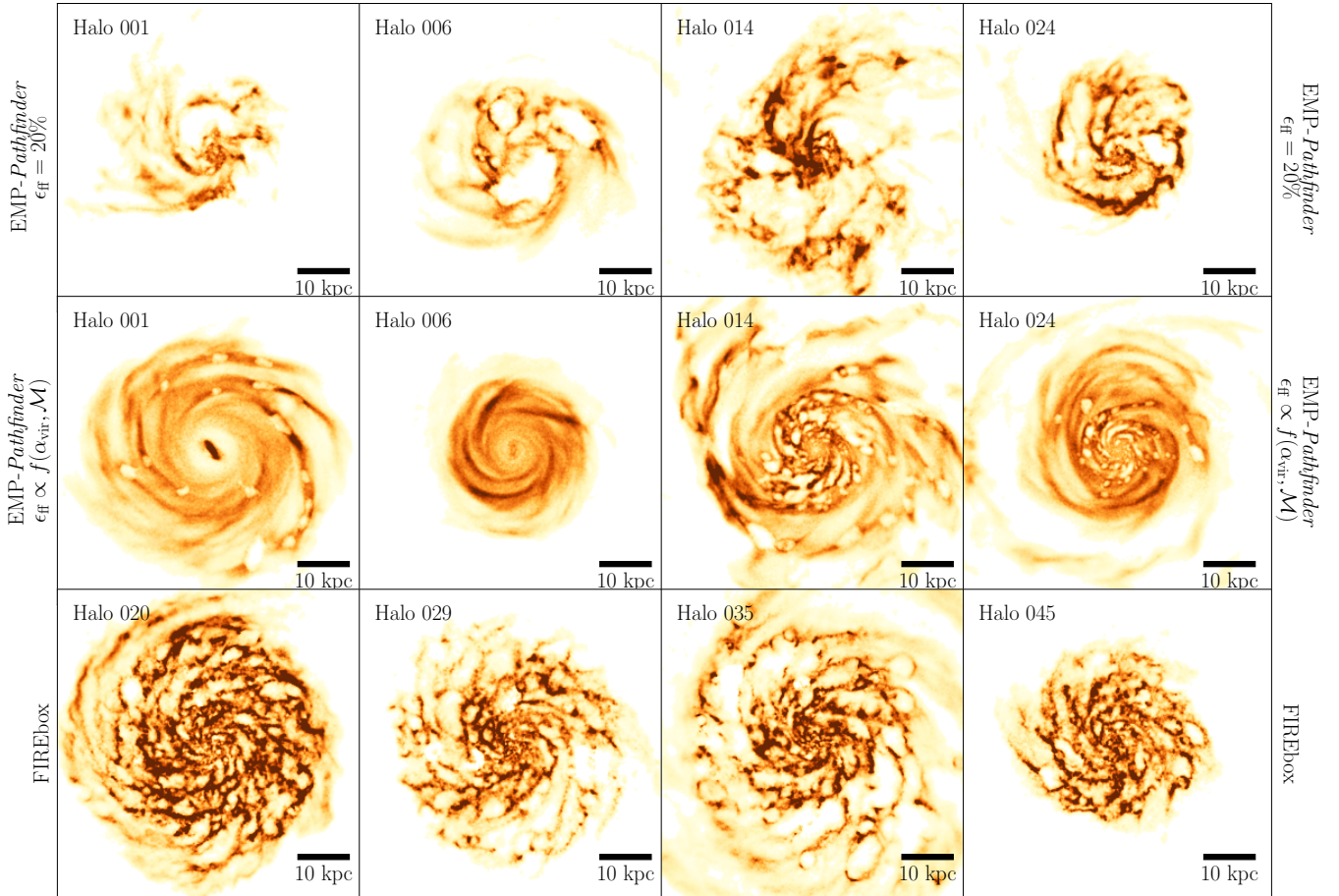


Figure 7. Face-on projection of the HI surface density, 60 kpc a side, for four example galaxies of each baryonic physics galaxy sub-set. From top to bottom, the maps show galaxies evolved with the *Pathfinder*-cSFE, *Pathfinder*-mffSFE (where the same galaxies have been chosen to highlight the differences) and FIREbox physics. These are the fiducial projections with a resolution of 80 pc and a density threshold of $7 \times 10^{19} \text{ cm}^{-2}$. The colourmap linearly scales with the gas surface density from light to dark brown at $10 M_{\odot} \text{ pc}^{-2}$. The white background colour indicates the regions where the HI surface density is below the threshold.

sion for each different physics sub-set of galaxies, we also perform one for the combined data set including all simulated galaxies, where we add an additional flag to denote the sub-grid physics model⁷ of the simulations.

It is important to stress that the small sample size of 46 galaxies in the combined sample necessarily limits the predictive strength of the RFR, especially when considering the different baryonic physics sub-samples. In those cases, the RFR offers an overview of features that could be important, and for which we have verified that the non-parametric morphological indicator shows a statistically significant, monotonic (anti-) correlation with the respective quantity using the Spearman rank correlation coefficient. To get a better handle on the uncertainty associated with the RFR, we determine the mean feature importances and their standard deviation via bootstrapping. Specifically, we generate 30 different train/test sets with the `train_test_split` function (using a `test_size` of 0.2) in `scikit-learn` by varying the seed of the random number generator,

⁷ While the only difference between *Pathfinder*-cSFE and *Pathfinder*-mffSFE is in the star formation sub-grid model, this flag does implicitly fold in differences between GIZMO and AREPO and their respective treatment of physical processes other than star formation and stellar feedback, in addition to those differences, for FIREbox.

which governs the division into train and test sample. Subsequently, we run 30 RFRs with different random number seeds on each training set, resulting in a total of 900 RFRs.

Figure 8 shows the results of the random forest regression for each sub-set, as well as the combined sample of simulated galaxies. For Gini, the most relevant features are R_{HI} and the mass of HI within R_{HI} and R_{gal} , which are strongly correlated (Figure 2). Since Gini measures the inequality in the density distribution, this is not surprising considering the median HI surface density profiles (Figure 3) of the gas discs. Especially for *Pathfinder*-mffSFE and FIREbox galaxies the median HI surface densities vary little in the central region before exponentially declining at $R \geq 0.8R_{\text{HI}}$, which in combination with the density cuts leads to a sharp contrast between high surface density pixels and those without. The median HI surface density of the *Pathfinder*-cSFE galaxies already declines gradually from the centre of the disc, which plausibly accounts for the feature importance of the average HI surface density within R_{HI} in predicting Gini for this sub-set of galaxies.

Considering the combined data-set, the most important features to predict the Smoothness are the average (central) total gas surface density and the central stellar surface density. These properties all show a mild anti-correlation with Smoothness, i.e. the denser the gas and the deeper the potential, the smoother the HI disc. Interestingly,

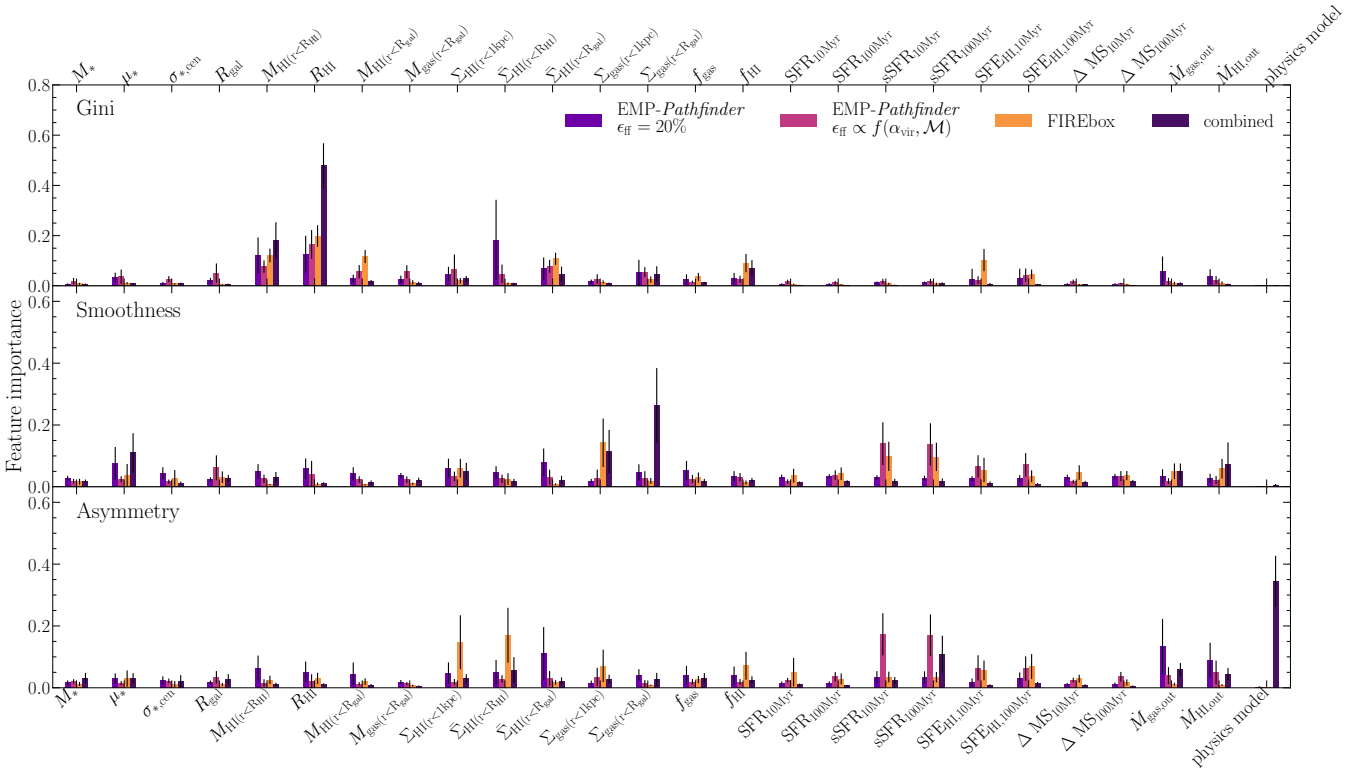


Figure 8. Results of the random forest regression for the Gini, Smoothness and Asymmetry parameters (top to bottom). Feature importance are shown in purple, magenta, orange and dark blue for the constant SFE EMP-Pathfinder, multi free-fall EMP-Pathfinder, FIREbox and the combined sample respectively. Bars show the mean feature importance, with error bars denoting the standard deviation, determined via bootstrapping of 30 random forest regressions on each of the 30 randomly selected sub-samples. The most important feature to predict the Asymmetry of HI discs in the combined data set is the sub-grid physics with which the galaxies were simulated.

this matches the findings of Davis et al. (2022) for the most important predictors for the Smoothness of the central molecular gas discs in a sample of local early- and late-type galaxies. In Davis et al. (2022) this is interpreted as a consequence of the dynamical suppression of fragmentation, where shear from the deeper central gravitational potential in high- μ_* galaxies inhibits fragmentation (see also Genzior et al. 2020, 2023a). The primary dependence on the central molecular gas surface density is also a consequence of the stars dominating the potential and gravitational stability (Davis et al. 2022). Our sample consists of star-forming, mostly disc-like galaxies, and the HI discs extend to 10s of kpc from the centre of the galaxy. It is therefore more likely that the Smoothness depends on these quantities (especially in the FIREbox and Pathfinder-cSFE cases), because these quantities determine where stars form and how effectively outflows can be driven and thus how porous the ISM becomes. For Pathfinder-mffSFE galaxies, the specific star formation rate averaged over both 10 and 100 Myr is selected as the most important feature, which shows a correlation with the Smoothness (i.e. galaxies that form more stars with respect to their total stellar mass have a less smooth HI disc). This is likely because in this sub-grid star formation model the SFR is less dependent on the gas density, because the ϵ_{ff} is set by the local turbulent properties instead. It will thus depend somewhat on the potential, as galaxies with higher- μ_* are likely to have a higher turbulent velocity dispersion (in the central regions) thereby inhibiting star formation somewhat. The dependence of the Smoothness of the FIREbox galaxies on the sSFR is likely the result of the strong primary dependence on the gas surface density, which governs the star formation activity in FIRE.

Asymmetry is where the feature importances between the individual galaxy sub-sets and for the combined data-set differ the most. The most important feature to predict the Asymmetry of HI discs for the combined set is the baryonic physics model (0.34 ± 0.08), highlighting that it is very sensitive to the subtle differences in star formation and feedback physics (and their consequences). This suggests, therefore, that the Asymmetry of HI discs could be a very promising observable to further our understanding of the baryonic physics at play in our Universe. The most important features for Pathfinder-cSFE galaxies are the outflow rates. They are correlated with the Asymmetry, i.e. stronger outflows lead to more asymmetric discs. For the Pathfinder-mffSFE galaxies, the sSFR is the most important, again showing a correlation with the Asymmetry. The (central) HI density is the most important feature for FIREbox galaxies, which is anti-correlated with the Asymmetry. This is perhaps counter-intuitive, as a higher surface density should lead to higher SFRs and thus more feedback. However, denser gas will be able to cool more efficiently and is more strongly gravitationally bound, thus making it harder to disturb. In short, the most important features to predict the Asymmetry of the HI discs all directly relate to the different physics models, where stars form and how effective the stellar feedback will be in affecting the gas distribution.

We repeat the RFR for the non-parametric indicators computed from maps at coarser resolution, with a higher density threshold and random inclinations $< 70^\circ$. Figure 9 shows the feature importances for predicting the Asymmetry of the combined dataset. Crucially, the physics model remains the most important feature (feature importances $0.34 \pm 0.08 - 0.48 \pm 0.12$) by far. The only qualitative

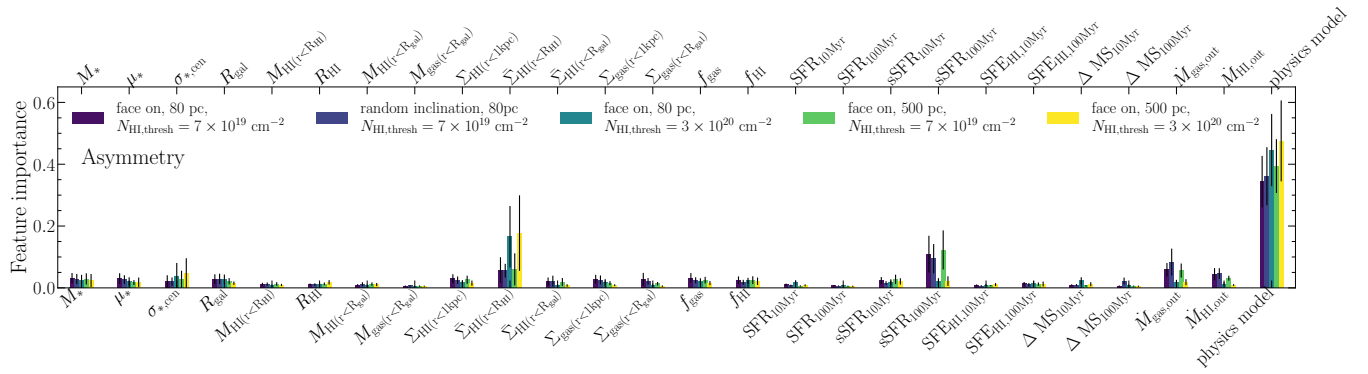


Figure 9. Results of the random forest regression trained on the combined data set, to identify the best predictor for the Asymmetry of the HI discs. Coloured bars and error bars show the mean and standard deviation determined via bootstrapping of performing 30 random forest regressions on each of the 30 randomly selected sub-samples. Different colours indicate the results of the random forest regression for the random inclination, different resolution and density threshold maps from which the non-parametric morphologies were determined. The physics model is selected as the most important feature in all cases and by a large margin.

difference between the feature importances for the different maps is the selection of average global surface density as the second most important feature (compared to the sSFR) for the high-density threshold maps. This can be understood as the morphologies of galaxies with lower surface densities are more strongly affected by the stricter cut.

To further validate our results of the strong dependence of the HI disc Asymmetry on the underlying baryonic physics model, we also perform the reverse test. We use the combined dataset, include Gini, Asymmetry and Smoothness in the list of potential features and perform a RFR to predict the (flag for the) baryonic physics model of the simulated galaxies. The results for this RFR are shown in Figure 10. In all cases, the Asymmetry is by far the most important feature to predict the baryonic physics model (feature importance in the range $0.41 \pm 0.12 - 0.53 \pm 0.13$), independent of the inclination, resolution, or density threshold of the maps on which the non-parametric morphological indicators were calculated. This lends further support to the Asymmetry being a promising observable in order to validate or disprove physics models by comparison to observations.

Although limited by the small numbers in our sample, this approach demonstrates the power of combining complex statistical models (machine learning) with simulations run with different baryonic physics models to learn more about their effects and highlight particularly promising observables. A similar approach was taken by Macciò et al. (2022) to compare galaxies from the Numerical Investigation of a Hundred Astrophysical Objects (NIHAO; Wang et al. 2015) suite, simulated with the same constant SFE but different density thresholds for star formation, to THINGS galaxies to establish which gas maps best match the observations. They used a deep neural network, trained on moon craters, to identify features on simulated and observed gas maps. They found that the number of features in maps from galaxies simulated with a density threshold of 80 atoms per cubic centimetre (the highest in their sample) yields the best agreement with THINGS galaxies. Since NIHAO also includes early stellar feedback and a cold ISM, it would be interesting to see where these galaxies fall in the Smoothness-Asymmetry parameter space discussed in Section 4 and here. Care must be taken when comparing with (more) galaxies simulated with different hydro-dynamical codes, as even the gas disc morphologies of individual galaxies simulated with very ‘similar’ sub-grid physics appear visually different, with the largest differences between Eulerian and Lagrangian codes (e.g. Kim et al. 2016; Hu et al. 2023). However, the results presented in this paper are in large part driven by differences between the two

EMP-Pathfinder sub-sets of galaxies, where numerics-wise everything beyond the differences in SFE is exactly the same, and should therefore be robust. None the less, the possibility that some of the differences between FIREbox and EMP-Pathfinder stem from subtle differences in the numerics between GIZMO and AREPO, rather than the differences in baryonic physics, cannot be excluded.

6 CONCLUDING REMARKS

In this paper, we analysed the properties of 46 Milky Way halo-mass galaxies from the EMP-Pathfinder suite of cosmological zoom-in simulations and the FIREbox cosmological volume at $z = 0$, with a focus on their HI disc properties. The sample comprises galaxies simulated with three different star formation models. This is because the EMP-Pathfinder galaxies were evolved to $z = 0$ once with a constant $\epsilon_{\text{ff}} = 20$ per cent and once with an environmentally-dependent, turbulence-based ϵ_{ff} ; the FIRE-2 model also features a constant $\epsilon_{\text{ff}} = 100$ per cent, but additionally requires the gas to be locally self-gravitating, Jeans unstable and molecular. All simulations include supernovae feedback and stellar winds from evolved stars, but only FIREbox includes a contribution from early stellar feedback i.e. the winds, radiation pressure, winds, photoelectric heating and photoionization by massive OB stars. Therefore, this set of simulations is ideally suited to assess the impact of small differences in the sub-grid baryonic physics on galaxy properties after self-consistent evolution across cosmic time. Our results can be summarised as follows.

- (i) Despite the similar halo masses, the galaxy stellar masses differ between the different baryonic physics sub-sets, though they are generally consistent with the large scatter of the stellar-to-halo mass relation; half of the Pathfinder-cSFE galaxies have lower and a quarter of the FIREbox galaxies have higher stellar masses compared to that of the Milky Way. Nonetheless, the HI-to-stellar mass fractions of each sub-set are consistent with those of the star-forming xGASS (Catinella et al. 2018) galaxies. Furthermore, all galaxies lie on the HI mass-size relation in good agreement with observations.
- (ii) The median HI surface density profiles differ in both shape and normalisation within the inner part of the HI disc ($< 0.8R_{\text{HI}}$), before following the characteristic exponential decline observed in the HI discs of local late-type galaxies.

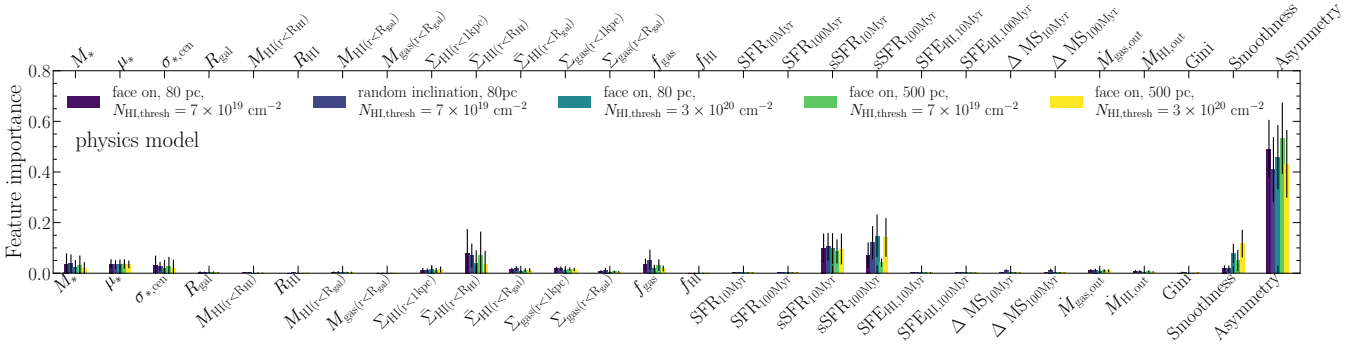


Figure 10. Results of the random forest regression to identify the best predictor for the baryonic physics model with which the galaxies were simulated. Coloured bars and error bars show the mean and standard deviation determined via bootstrapping of performing 30 random forest regressions on each of the 30 randomly selected sub-samples. Different colours indicate the results of the random forest regression for the random inclination, different resolution and density threshold maps from which the non-parametric morphologies were determined. The Asymmetry is selected as the most important feature in all cases and by a large margin.

- (iii) The HI discs of *Pathfinder*-cSFE galaxies are consistently thicker compared to the *Pathfinder*-mffSFE galaxies, to FIREbox galaxies, and to the observed THINGS galaxies (Bacchini et al. 2019), highlighting that a cold ISM might be a necessary, but not a sufficient condition to reproduce the thin gas discs observed in the local Universe.
- (iv) The HI disc morphologies, as quantified by the non-parametric morphological indicators Smoothness and Asymmetry, differ significantly between the different galaxy sub-sets. The *Pathfinder*-mffSFE galaxies have the smoothest and most rotationally symmetric HI discs, the *Pathfinder*-cSFE simulations the most asymmetric discs with large low-density areas, while the FIREbox discs have very similar morphologies (narrow range in Asymmetry and Smoothness), with Asymmetries between those of the *Pathfinder*-mffSFE and *Pathfinder*-cSFE galaxies.
- (v) Random forest regression selects the baryonic physics model as the most important feature to predict the Asymmetry of the HI discs, and vice-versa the Asymmetry (followed by the specific star formation rate) is the most important feature for predicting the baryonic physics model. This further highlights how sensitive the gas disc morphologies are to subtle differences in the baryonic physics and suggests their Asymmetry could be a powerful observable to better constrain the physics at play in the local Universe.

Our work demonstrates the sensitivity of gas disc morphologies to underlying star formation and feedback physics. However, to gain a more complete picture of their impact on galaxy evolution, a more thorough exploration including an entire range of halo masses, using more simulations with different physics, is required. For example, despite the different stellar feedback in EMP-*Pathfinder* and FIREbox, the implementation of the feedback injection is similar, as the EMP-*Pathfinder* implementation follows the FIRE-2 (Hopkins et al. 2018) mechanical feedback coupling algorithm. Thus, it would be informative to see how different implementations, such as blast-wave feedback (e.g. Stinson et al. 2010) or kinetic feedback (e.g. AURIGA; Grand et al. 2017), affect the distributions of Asymmetry and Smoothness. Furthermore, since our results remain robust even for coarse resolutions of 500 pc, this potentially enables an exploration of how the HI disc morphology of galaxies is affected by AGN feedback, by drawing on cosmological simulations that also include AGN feedback (e.g. EAGLE and IllustrisTNG, which have a resolution of several hundred pc). Complementarily, a large sample of high-resolution observations of HI disc morphologies from the

SKA and its precursors (e.g. MHONGOOSE) would help validate or disprove these different physics models.

ACKNOWLEDGEMENTS

We thank an anonymous referee for their helpful and constructive report. We thank Kai Polsterer for his input on machine learning methods and feature importance. JG gratefully acknowledges financial support from the Swiss National Science Foundation (grant no CRSII5_193826). RF acknowledges financial support from the Swiss National Science Foundation (grant nos. 194814, 200021_188552). MRC gratefully acknowledges the Canadian Institute for Theoretical Astrophysics (CITA) National Fellowship for partial support. This work was supported by the Natural Sciences and Engineering Research Council of Canada (NSERC). STG gratefully acknowledges the generous and invaluable support of the Klaus Tschira Foundation, in addition to funding from the European Research Council (ERC) under the European Union’s Horizon 2020 research and innovation programme via the ERC Starting Grant MUSTANG (grant agreement number 714907). AW received support from: NSF via CAREER award AST-2045928 and grant AST-2107772; NASA ATP grant 80NSSC20K0513; HST grants AR-15809, GO-15902, GO-16273 from STScI. JMDK gratefully acknowledges funding from the DFG through an Emmy Noether Research Group (grant number KR4801/1-1) and from the European Research Council (ERC) under the European Union’s Horizon 2020 research and innovation programme via the ERC Starting Grant MUSTANG (grant agreement number 714907). COOL Research DAO is a Decentralised Autonomous Organisation supporting research in astrophysics aimed at uncovering our cosmic origins. Support for PFH was provided by NSF Research Grants 1911233, 20009234, 2108318, NSF CAREER grant 1455342, NASA grants 80NSSC18K0562, HST-AR-15800. JM is funded by the Hirsch Foundation.

The EMP-*Pathfinder* production runs were run on the Graham supercomputing cluster from Compute Ontario, and on the BinAc cluster from the University of Tübingen. The research was enabled in part by support provided by Compute Ontario (<https://www.computeontario.ca>) and Compute Canada (<https://www.computecanada.ca>). The authors acknowledge support by the High Performance and Cloud Computing Group at the Zentrum für Datenverarbeitung of the University of Tübingen, the state of Baden-Württemberg through bwHPC and the German Research Foundation (DFG) through grant no. INST 37/935-1 FUGG. We acknowledge

PRACE for awarding us access to MareNostrum at the Barcelona Supercomputing Center (BSC), Spain. This work was supported in part by a grant from the Swiss National Supercomputing Centre (CSCS) under project IDs s697 and s698. We acknowledge access to Piz Daint at the Swiss National Supercomputing Centre, Switzerland under the University of Zurich's share with the project ID uzh18. This work made use of infrastructure services provided by S3IT (www.s3it.uzh.ch), the Service and Support for Science IT team at the University of Zurich.

Software: This work made use of the python packages `h5py` (Collette et al. 2023), `jupyter-notebooks` (Kluyver et al. 2016), `matplotlib` (Hunter 2007), `NumPy` (Harris et al. 2020), `pandas` (Wes McKinney 2010; pandas development team 2020), `scikit-learn` (Pedregosa et al. 2011), and `SciPy` (Virtanen et al. 2020).

DATA AVAILABILITY

The data supporting the plots in this article will be shared on reasonable request to the corresponding author.

REFERENCES

- Abraham R. G., Valdes F., Yee H. K. C., van den Bergh S., 1994, *ApJ*, **432**, 75
- Abraham R. G., Tanvir N. R., Santiago B. X., Ellis R. S., Glazebrook K., van den Bergh S., 1996, *MNRAS*, **279**, L47
- Bacchini C., Fraternali F., Iorio G., Pezzulli G., 2019, *A&A*, **622**, A64
- Bacchini C., Fraternali F., Iorio G., Pezzulli G., Marasco A., Nipoti C., 2020, *A&A*, **641**, A70
- Bahé Y. M., et al., 2016, *MNRAS*, **456**, 1115
- Barnes A. T., Longmore S. N., Battersby C., Bally J., Kruijssen J. M. D., Henshaw J. D., Walker D. L., 2017, *MNRAS*, **469**, 2263
- Begum A., Chengalur J. N., Karachentsev I. D., Sharina M. E., Kaisin S. S., 2008, *MNRAS*, **386**, 1667
- Benincasa S. M., et al., 2020, *MNRAS*, **497**, 3993
- Benítez-Llambay A., Navarro J. F., Frenk C. S., Ludlow A. D., 2018, *MNRAS*, **473**, 1019
- Bigiel F., Blitz L., 2012, *ApJ*, **756**, 183
- Bigiel F., Leroy A., Walter F., Brinks E., de Blok W. J. G., Madore B., Thornley M. D., 2008, *AJ*, **136**, 2846
- Bland-Hawthorn J., Gerhard O., 2016, *ARA&A*, **54**, 529
- Blitz L., Rosolowsky E., 2006, *ApJ*, **650**, 933
- Boomsma R., Oosterloo T. A., Fraternali F., van der Hulst J. M., Sancisi R., 2008, *A&A*, **490**, 555
- Broeils A. H., Rhee M. H., 1997, *A&A*, **324**, 877
- Burkhart B., 2018, *ApJ*, **863**, 118
- Catinella B., et al., 2018, *Monthly Notices of the Royal Astronomical Society*, **476**, 875
- Cautun M., et al., 2020, *MNRAS*, **494**, 4291
- Chevance M., et al., 2020, *MNRAS*, **493**, 2872
- Chevance M., et al., 2022, *MNRAS*, **509**, 272
- Chevance M., Krumholz M. R., McLeod A. F., Ostriker E. C., Rosolowsky E. W., Sternberg A., 2023, in Inutsuka S., Aikawa Y., Muto T., Tomida K., Tamura M., eds, *Astronomical Society of the Pacific Conference Series* Vol. 534, *Protostars and Planets VII*. p. 1 ([arXiv:2203.09570](https://arxiv.org/abs/2203.09570)), doi:10.48550/arXiv.2203.09570
- Collette A., et al., 2023, `h5py/h5py`: 3.8.0-aarch64-wheels, doi:10.5281/zenodo.7568214, <https://doi.org/10.5281/zenodo.7568214>
- Conselice C. J., 2003, *ApJS*, **147**, 1
- Crain R. A., van de Voort F., 2023, *ARA&A*, **61**, 473
- Davis M., Efstathiou G., Frenk C. S., White S. D. M., 1985, *ApJ*, **292**, 371
- Davis T. A., et al., 2014, *MNRAS*, **444**, 3427
- Davis T. A., et al., 2022, *MNRAS*, **512**, 1522
- Deg N., Perron-Cormier M., Spekkens K., Glowacki M., Blyth S. L., Hank N., 2023, *MNRAS*, **523**, 4340
- Dolag K., Borgani S., Murante G., Springel V., 2009, *MNRAS*, **399**, 497
- Donalek C., et al., 2013, in 2013 IEEE International Conference on Big Data. pp 35–41, doi:10.1109/BigData.2013.6691731
- Evans N. J., Kim J.-G., Ostriker E. C., 2022, *ApJ*, **929**, L18
- Faucher-Giguère C.-A., Lidz A., Zaldarriaga M., Hernquist L., 2009, *ApJ*, **703**, 1416
- Federrath C., Klessen R. S., 2012, *ApJ*, **761**, 156
- Feldmann R., et al., 2023, *MNRAS*, **522**, 3831
- Gebek A., et al., 2023, *MNRAS*, **521**, 5645
- Gensior J., Kruijssen J. M. D., 2021, *MNRAS*, **500**, 2000
- Gensior J., Kruijssen J. M. D., Keller B. W., 2020, *MNRAS*, **495**, 199
- Gensior J., Davis T. A., Bureau M., Kruijssen J. M. D., Cappellari M., Ruffa I., Williams T. G., 2023a, *MNRAS* submitted
- Gensior J., Feldmann R., Mayer L., Wetzel A., Hopkins P. F., Faucher-Giguère C.-A., 2023b, *MNRAS*, **518**, L63
- Gill S. P. D., Knebe A., Gibson B. K., 2004, *MNRAS*, **351**, 399
- Grand R. J. J., et al., 2017, *MNRAS*, **467**, 179
- Guedes J., Callegari S., Madau P., Mayer L., 2011, *ApJ*, **742**, 76
- Haardt F., Madau P., 2012, *ApJ*, **746**, 125
- Harris C. R., et al., 2020, *Nature*, **585**, 357
- Hennebelle P., Chabrier G., 2011, *ApJ*, **743**, L29
- Holwerda B. W., Pirzkal N., de Blok W. J. G., Bouchard A., Blyth S. L., van der Heyden K. J., Elson E. C., 2011a, *MNRAS*, **416**, 2401
- Holwerda B. W., Pirzkal N., de Blok W. J. G., Bouchard A., Blyth S. L., van der Heyden K. J., Elson E. C., 2011b, *MNRAS*, **416**, 2415
- Holwerda B. W., et al., 2023, *MNRAS*, **521**, 1502
- Hopkins P. F., 2015, *MNRAS*, **450**, 53
- Hopkins P. F., Narayanan D., Murray N., 2013, *MNRAS*, **432**, 2647
- Hopkins P. F., Kereš D., Oñorbe J., Faucher-Giguère C.-A., Quataert E., Murray N., Bullock J. S., 2014, *MNRAS*, **445**, 581
- Hopkins P. F., et al., 2018, *MNRAS*, **480**, 800
- Hu C.-Y., et al., 2023, *ApJ*, **950**, 132
- Hunter J. D., 2007, *Computing in Science & Engineering*, **9**, 90
- Janowiecki S., Catinella B., Cortese L., Saintonge A., Wang J., 2020, *MNRAS*, **493**, 1982
- Jarvis M., et al., 2016, in MeerKAT Science: On the Pathway to the SKA. p. 6 ([arXiv:1709.01901](https://arxiv.org/abs/1709.01901)), doi:10.22323/1.277.0006
- Keller B. W., Kruijssen J. M. D., Chevance M., 2022, *MNRAS*, **514**, 5355
- Kennicutt Jr. R. C., 1998, *ApJ*, **498**, 541
- Kim J.-h., et al., 2016, *ApJ*, **833**, 202
- Kim J., et al., 2022, *MNRAS*, **516**, 3006
- Kluyver T., et al., 2016, in Loizides F., Schmidt B., eds, *Positioning and Power in Academic Publishing: Players, Agents and Agendas*. pp 87 – 90
- Knollmann S. R., Knebe A., 2009, *ApJS*, **182**, 608
- Koribalski B. S., et al., 2020, *Ap&SS*, **365**, 118
- Kretschmer M., Teyssier R., 2020, *MNRAS*, **492**, 1385
- Kruijssen J. M. D., Longmore S. N., Elmegreen B. G., Murray N., Bally J., Testi L., Kennicutt R. C., 2014, *MNRAS*, **440**, 3370
- Kruijssen J. M. D., Pfeffer J. L., Crain R. A., Bastian N., 2019, *MNRAS*, **486**, 3134
- Krumholz M. R., Gnedin N. Y., 2011, *ApJ*, **729**, 36
- Krumholz M. R., McKee C. F., 2005, *ApJ*, **630**, 250
- Krumholz M. R., Dekel A., McKee C. F., 2012, *ApJ*, **745**, 69
- Lelli F., Verheijen M., Fraternali F., 2014, *MNRAS*, **445**, 1694
- Lelli F., McGaugh S. S., Schombert J. M., 2016, *AJ*, **152**, 157
- Leroy A. K., Walter F., Brinks E., Bigiel F., de Blok W. J. G., Madore B., Thornley M. D., 2008, *AJ*, **136**, 2782
- Leroy A. K., et al., 2021, *ApJS*, **257**, 43
- Longmore S. N., et al., 2013, *MNRAS*, **429**, 987
- Lotz J. M., Primack J., Madau P., 2004, *AJ*, **128**, 163
- Macciò A. V., Ali-Dib M., Vulcanovic P., Al Noori H., Walter F., Krieger N., Buck T., 2022, *MNRAS*, **512**, 2135
- Maddox N., et al., 2021, *A&A*, **646**, A35
- Marinacci F., Grand R. J. J., Pakmor R., Springel V., Gómez F. A., Frenk C. S., White S. D. M., 2017, *MNRAS*, **466**, 3859

- Naab T., Ostriker J. P., 2017, *ARA&A*, 55, 59
- Nuñez-Castiñeyra A., Nezri E., Devriendt J., Teyssier R., 2021, *MNRAS*, 501, 62
- Obreschkow D., Croton D., De Lucia G., Khochfar S., Rawlings S., 2009, *ApJ*, 698, 1467
- Orr M. E., Fielding D. B., Hayward C. C., Burkhart B., 2022, *ApJ*, 924, L28
- Padoan P., Nordlund Å., 2011, *ApJ*, 730, 40
- Patra N. N., 2020, *MNRAS*, 499, 2063
- Pedregosa F., et al., 2011, *Journal of Machine Learning Research*, 12, 2825
- Pfeffer J., Kruijssen J. M. D., Crain R. A., Bastian N., 2018, *MNRAS*, 475, 4309
- Pillepich A., et al., 2019, *MNRAS*, 490, 3196
- Popping G., Somerville R. S., Trager S. C., 2014, *MNRAS*, 442, 2398
- Querejeta M., et al., 2019, *A&A*, 625, A19
- Rajohnson S. H. A., et al., 2022, *MNRAS*, 512, 2697
- Randriamampandry T. H., Wang J., Mogotsi K. M., 2021, *ApJ*, 916, 26
- Reina-Campos M., Keller B. W., Kruijssen J. M. D., Gensior J., Trujillo-Gomez S., Jeffreson S. M. R., Pfeffer J. L., Sills A., 2022, *MNRAS*, 512, 2697
- Rodriguez-Gomez V., et al., 2019, *MNRAS*, 483, 4140
- Saintonge A., Catinella B., 2022, *ARA&A*, 60, 319
- Schaye J., et al., 2015, *MNRAS*, 446, 521
- Semenov V. A., Kravtsov A. V., Gnedin N. Y., 2021, *ApJ*, 918, 13
- Silich S., Tenorio-Tagle G., 2001, *ApJ*, 552, 91
- Smith B. D., et al., 2017, *MNRAS*, 466, 2217
- Smith M. C., Bryan G. L., Somerville R. S., Hu C.-Y., Teyssier R., Burkhart B., Hernquist L., 2021, *MNRAS*, 506, 3882
- Somerville R. S., Davé R., 2015, *ARA&A*, 53, 51
- Springel V., 2010, *MNRAS*, 401, 791
- Springel V., White S. D. M., Tormen G., Kauffmann G., 2001, *MNRAS*, 328, 726
- Stevens A. R. H., Diemer B., Lagos C. d. P., Nelson D., Obreschkow D., Wang J., Marinacci F., 2019, *MNRAS*, 490, 96
- Stinson G. S., Bailin J., Couchman H., Wadsley J., Shen S., Nickerson S., Brook C., Quinn T., 2010, *MNRAS*, 408, 812
- Stinson G. S., Brook C., Macciò A. V., Wadsley J., Quinn T. R., Couchman H. M. P., 2013, *MNRAS*, 428, 129
- Sun J., et al., 2023, *ApJ*, 945, L19
- Swaters R. A., van Albada T. S., van der Hulst J. M., Sancisi R., 2002, *A&A*, 390, 829
- Tacconi L. J., Genzel R., Sternberg A., 2020, *ARA&A*, 58, 157
- Thorp M. D., Bluck A. F. L., Ellison S. L., Maiolino R., Selscice C. J., Hani M. H., Bottrell C., 2021, *MNRAS*, 507, 886
- Usero A., et al., 2015, *AJ*, 150, 115
- Utomo D., et al., 2018, *ApJ*, 861, L18
- Virtanen P., et al., 2020, *Nature Methods*, 17, 261
- Walter F., Brinks E., de Blok W. J. G., Bigiel F., Kennicutt Robert C. J., Thornley M. D., Leroy A., 2008, *AJ*, 136, 2563
- Wang J., et al., 2013, *MNRAS*, 433, 270
- Wang J., et al., 2014, *MNRAS*, 441, 2159
- Wang L., Dutton A. A., Stinson G. S., Macciò A. V., Penzo C., Kang X., Keller B. W., Wadsley J., 2015, *MNRAS*, 454, 83
- Wang J., Koribalski B. S., Serra P., van der Hulst T., Roychowdhury S., Kamphuis P., Chengalur J. N., 2016, *MNRAS*, 460, 2143
- Wang J., Catinella B., Saintonge A., Pan Z., Serra P., Shao L., 2020, *ApJ*, 890, 63
- Weinberger R., Springel V., Pakmor R., 2020, *ApJS*, 248, 32
- Wes McKinney 2010, in *Stéfan van der Walt Jarrod Millman eds, Proceedings of the 9th Python in Science Conference*. pp 56 – 61, doi:10.25080/Majors-92bf1922-00a
- de Blok W. J. G., et al., 2016, in *MeerKAT Science: On the Pathway to the SKA*. p. 7 (arXiv:1709.08458), doi:10.22323/1.277.0007
- de los Reyes M. A. C., Kennicutt Jr. R. C., 2019, *ApJ*, 872, 16
- pandas development team T., 2020, *pandas-dev/pandas: Pandas*, doi:10.5281/zenodo.3509134, https://doi.org/10.5281/zenodo.3509134

APPENDIX A: COMPARING DIFFERENT MODELS FOR OBTAINING HI AND H₂ FRACTIONS FROM THE NEUTRAL GAS

As discussed in Section 2.3.1, we use two different models to infer the ‘true’ HI content from the neutral gas fraction in the EMP-*Pathfinder* and FIREBOX galaxies. The HI fraction of EMP-*Pathfinder* galaxies is calculated using the empirical, pressure-based model of Blitz & Rosolowsky (2006). For FIREBOX galaxies, we use the Krumholz & Gnedin (2011) model, based on idealised cloud simulations, which is also used to estimate the H₂ fraction at run time in FIRE. The use of two different models is motivated by attempting to match the observed density threshold of $\sim 10 M_{\odot} \text{pc}^{-2}$ at which Σ_{HI} saturates and above which gas becomes molecular (e.g. Blitz & Rosolowsky 2006; Bigiel et al. 2008; Leroy et al. 2008). Calculating the HI fraction with the respective non-fiducial model leads to higher HI abundances that result in surface densities in excess of $20 M_{\odot} \text{pc}^{-2}$ for many galaxies in the respective sub-set. This is particularly visible for FIREBOX galaxies in the left panel of Figure A3. In this Appendix, we show versions of Figures 1 – 4 and Figure 6 where f_{HI} has been calculated with the same model for all simulated galaxies for both the Blitz & Rosolowsky (2006) and Krumholz & Gnedin (2011) model in Figures A1 – A5.

The main difference in f_{HI} , as computed from the different models, is an increase in the total HI mass, i.e. shifting to higher HI-to-stellar mass ratios, driven by an increase in central HI for the non-fiducial model. Therefore, these galaxies are on average more offset from the HI main sequence (see Figure A1) and the HI mass-size relation (see Figure A2), because the HI scale radius, R_{HI} is not sensitive to the enhanced HI fraction in the central regions.

Similarly, the median central Σ_{HI} of the different physics simulated galaxy sub-sets increases by a factor of 2 (EMP-*Pathfinder*) to 2.5 (FIREBOX) compared to the fiducial model (Figure A3). While the shape of the surface density profile remains similar for the EMP-*Pathfinder* galaxies, independent of the H₂ model, it changes significantly for the FIREBOX galaxies. With the pressure-based Blitz & Rosolowsky (2006) model, the median Σ_{HI} declines as a function of radius at all radii, contrary to the behaviour with the FIREBOX-fiducial Krumholz & Gnedin (2011), where Σ_{HI} is approximately constant in the central regions, before declining for $R > 0.3R_{\text{HI}}$.

The effect of the different HI models on calculating the scale height is negligible for the individual galaxy sub-sets (Figure A4). In the non-fiducial case, h_{HI} becomes slightly smaller due to the enhanced HI density. This results in the *Pathfinder*-mffSFE and FIREBOX median scale heights becoming more offset from each other, albeit still within the range of the THINGS galaxies, when comparing h_{HI} exclusively calculated via the Blitz & Rosolowsky (2006) model.

Finally, we show the results of calculating the non-parametric morphological indicators from the two different HI model gas surface density projections in Figure A5. The sub-sets of galaxies simulated with different physics remain clearly separated in the Smoothness-Asymmetry parameter space in both cases, particularly when using the Blitz & Rosolowsky (2006) model for all galaxies. The non-parametric HI morphologies of the FIREBOX galaxies are the most affected by the HI model, with nearly all galaxies clustered tightly around $A = 0.9$ when using the non-fiducial Blitz & Rosolowsky (2006) model. The *Pathfinder*-cSFE galaxies become a little less smooth (median S shifting from 0.26 to 0.29), and their trend between Smoothness and Asymmetry is no longer statistically significant at the $p < 0.01$ level when using the Krumholz & Gnedin (2011) model, while the effect on the HI morphologies of the *Pathfinder*-mffSFE galaxies is negligible.

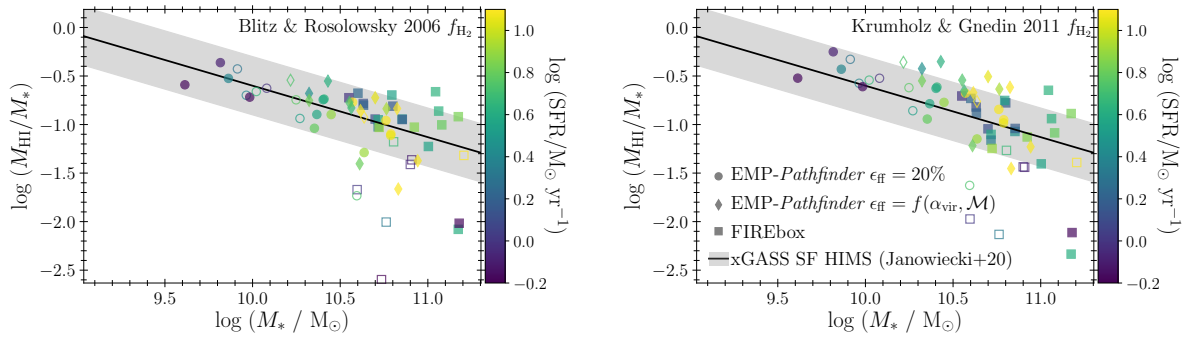


Figure A1. HI-to-stellar mass fraction as a function of stellar mass of the simulated galaxies in our sample. The left and right panels show the simulation data with the HI fraction calculated using the pressure-based [Blitz & Rosolowsky \(2006\)](#) model and the [Krumholz & Gnedin \(2011\)](#) formalism, respectively. The data are colour-coded by their star formation rate, with different symbols denoting the different sub-grid physics samples. Empty symbols denote the galaxies excluded from further analysis, due to interactions. The data are overlotted on the HI main sequence relation of the star-forming xGASS ([Catinella et al. 2018](#)) galaxies from [Janowiecki et al. \(2020\)](#) shown as a solid black line, and the 0.3 dex uncertainty in grey shading. The global HI content of galaxies is larger in case of the non-fiducial model. *Pathfinder*-mffSFE is affected the most, with shifts of ~ 0.3 dex, moving 6 (7) galaxies above the 0.3 dex scatter on the xGASS HI main sequence when calculating the HI fraction using [Krumholz & Gnedin \(2011\)](#).

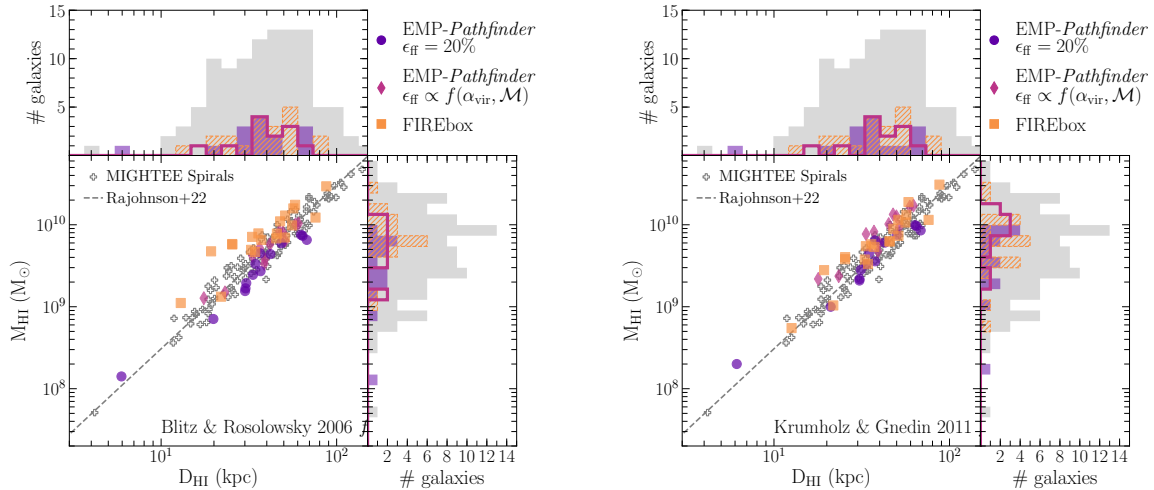


Figure A2. HI mass-size relation for the galaxies in our sample. The left and right panels show the simulation data with the HI fraction calculated using the pressure-based [Blitz & Rosolowsky \(2006\)](#) model and the [Krumholz & Gnedin \(2011\)](#) formalism, respectively. Purple circles denote the *Pathfinder*-cSFE galaxies, magenta diamonds denote the *Pathfinder*-mffSFE galaxies, and orange squares denote the FIREbox galaxies. Histograms show the marginal distributions for each indicator and galaxy sub-set. The grey dashed line shows the HI mass-size relation from MIGHTEE ([Rajohnson et al. 2022](#)). Galaxies tend to be more offset from the HI mass-size relation with the non-fiducial model, which is especially pronounced for the smaller FIREbox discs and the *Pathfinder*-mffSFE galaxies.

In summary, our tests show that while the global HI mass of the galaxies, and to a lesser extent its distribution within the galaxy, changes depending on the model, our qualitative conclusions remain robust irrespective of the model. Crucially, this is especially the case for the trends of the HI disc morphologies and the clear separation between the galaxy sub-sets simulated with different physics in the Smoothness-Asymmetry parameter space.

APPENDIX B: ADDITIONAL GINI, SMOOTHNESS AND ASYMMETRY PLOTS FOR DIFFERENT DENSITY THRESHOLDS AND RESOLUTIONS

In this Appendix, we show the non-parametric morphological parameter measurements computed from maps with a higher density

column threshold of $3 \times 10^{20} \text{ cm}^{-2}$, coarser resolution and random inclinations in Figures B1 – B5. Comparing Figure 6 with Figure B1, shows that a higher column density cut does not affect the trends of the Asymmetry measurements strongly. It does lead to larger rotational asymmetries, the differences are more pronounced for the FIREbox and *Pathfinder*-cSFE galaxies (the smooth and symmetric sub-set of *Pathfinder*-mffSFE galaxies remains very smooth and symmetric), but differences are of order ~ 20 per cent. The Smoothness parameter is far more affected by the density cut. The difference is strongest for the *Pathfinder*-cSFE galaxies, with Smoothness increasing by approximately a factor of 2 across the sample, i.e. the resultant maps are far less smooth than the fiducial ones. FIREbox galaxies are less affected, the Smoothness increases by a factor of 1.5-2 for 5 galaxies only. The remainder of the FIREbox galaxies and

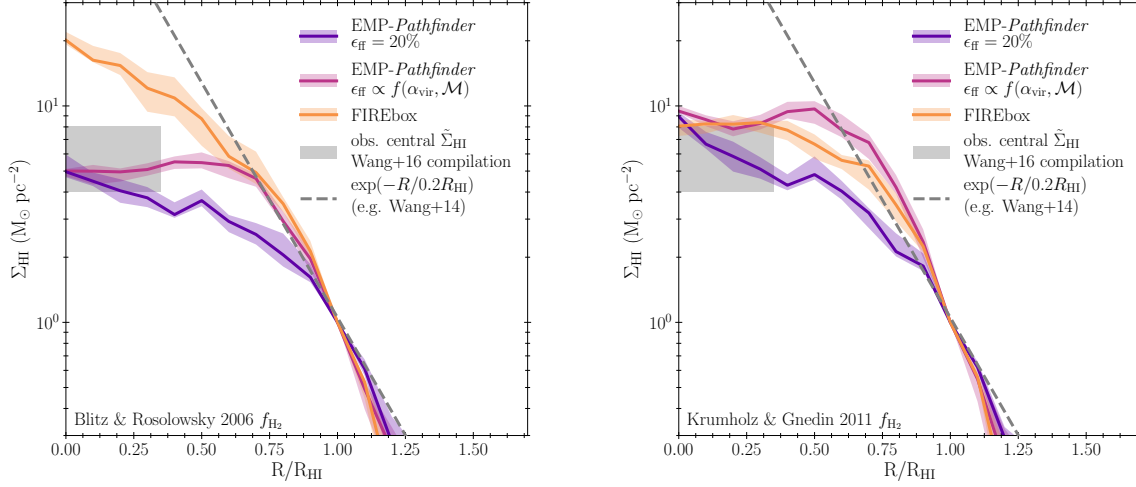


Figure A3. Radial HI gas surface density profiles. The left and right panels show the simulation data with the HI fraction calculated using the pressure-based Blitz & Rosolowsky (2006) model and the Krumholz & Gnedin (2011) formalism, respectively. Coloured lines and shaded regions denote the median and the error on the median, determined via bootstrapping, of each different baryonic physics sub-sample, respectively, with the Wang et al. (2014) exponential fit to the outer regions of observed HI surface density profiles overplotted as a grey-dashed line. For comparison, the grey shaded box indicates the central range of the median Σ_{HI} from 8 different observational samples, compiled by Wang et al. (2016). The median central surface densities reached by the simulated galaxy samples are a factor of ≥ 2 larger for the non-fiducial model, this is particularly pronounced for the FIREbox galaxies with a median Σ_{HI} of $20 \text{ M}_{\odot} \text{ pc}^{-2}$. When using the Blitz & Rosolowsky (2006) model, the median HI surface density radial profile of FIREbox galaxies continuously declines as a function of radius, as opposed to remaining approximately constant to $0.3R/R_{\text{HI}}$, before declining with the fiducial Krumholz & Gnedin (2011) model.

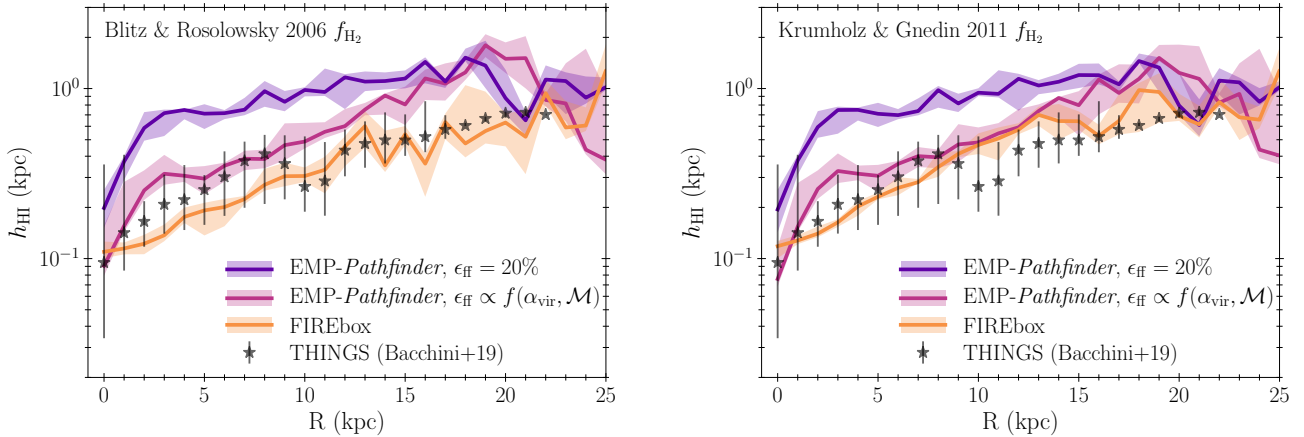


Figure A4. Radial profiles of the HI disc scale heights of the simulated galaxies, measured by fitting a Gaussian to the vertical volume density distribution in kpc bins. The left and right panels show the simulation data with the HI fraction calculated using the pressure-based Blitz & Rosolowsky (2006) model and the Krumholz & Gnedin (2011) formalism, respectively. Coloured lines and shaded regions denote the median and the error on the median, determined via bootstrapping, of each different baryonic physics subsample, respectively, with the THINGS scale heights (Bacchini et al. 2019) overplotted as black stars. The HI model has a negligible impact on the measured scale heights. They are marginally smaller when measured from the HI estimate obtained via the non-fiducial model, due to the larger HI surface densities in that case.

the *Pathfinder*-mffSFE galaxies experiences an order 0.01 increase in Smoothness. Gini remains largely unaffected by the increased surface density threshold. The scatter is slightly reduced, with the minimum values increasing from ~ 0.60 to 0.65 .

To test the effect of resolution, we smoothed the maps to a resolution of 500 pc using a Gaussian smoothing kernel, and subsequently regrid them such that the full-width-half-maximum still corresponds to approximately 4 pixels prior to computing the non-parametric morphological indicators. Figures B2 and B3 show the

results for the fiducial and the higher column density cut, respectively. The coarser resolution makes the gas distributions smoother and more symmetric, i.e. results in ~ 50 per cent smaller Smoothness, and lower Asymmetry values. The change in Asymmetry is most pronounced for FIREbox galaxies, where the Asymmetry decreases by up to 30 per cent. Since the Smoothness and Asymmetry *Pathfinder*-mffSFE galaxies are the least affected by the smoothing, it increases the overlap between FIREbox and *Pathfinder*-mffSFE galaxies.

Finally, we test the effect of inclination. Figure B4 shows the me-

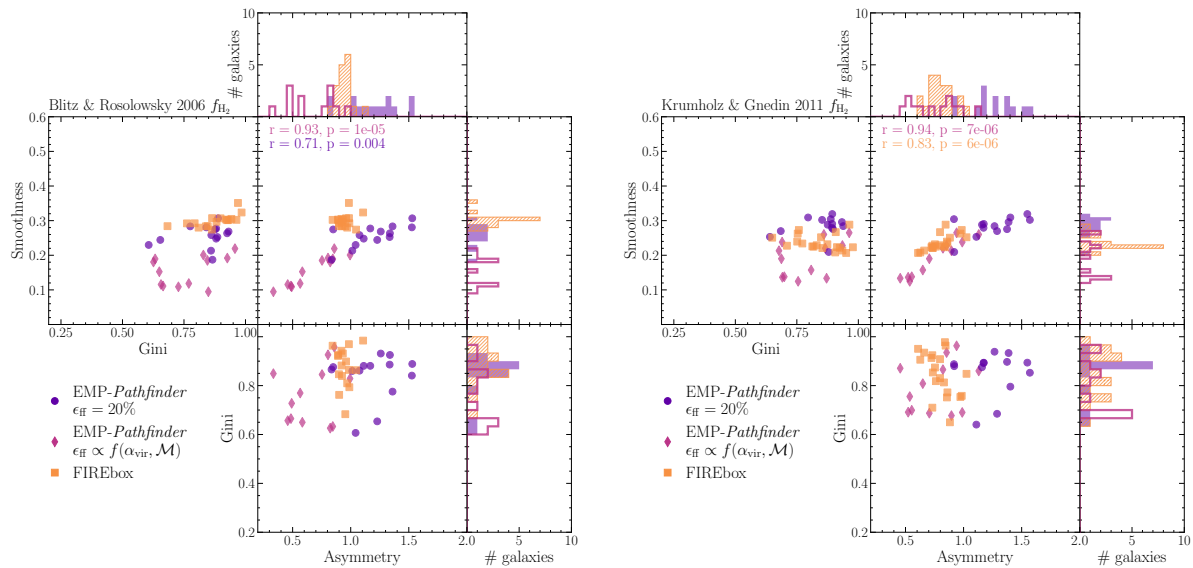


Figure A5. HI morphology as classified by the median non-parametric morphological indicators Smoothness, Gini and Asymmetry (plotted against each other in the three main panels), measured from face-on HI surface density projections of the galaxies with a resolution of 80 pc and column density threshold of $7 \times 10^{19} \text{ cm}^{-2}$. The left and right panels show the simulation data with the HI fraction calculated using the pressure-based [Blitz & Rosolowsky \(2006\)](#) model and the [Krumholz & Gnedin \(2011\)](#) formalism, respectively. Purple circles denote the *Pathfinder*-cSFE galaxies, while magenta diamonds denote the *Pathfinder*-mffSFE galaxies, and orange squares denote the FIREbox galaxies. Histograms show the marginal distributions for each indicator and galaxy sub-set. If a statistically significant correlation between two non-parametric morphological indicators is present, the Spearman rank correlation coefficient and p -value are included in the panels, colour indicating which simulated galaxy sub-set they apply to. The overall trends and segregation of the different physics simulated galaxy sub-sets remain the same, irrespective of how the HI fraction was calculated. The main difference occurs for FIREbox galaxies, which are shifted to higher Smoothness and show a much narrower range of Asymmetries when using the [Blitz & Rosolowsky \(2006\)](#) model.

dian Gini, Asymmetry and Smoothness measurements for each simulated galaxy computed on the fiducial maps with inclinations $< 70^\circ$. Grey error bars range from the minimum to the maximum value. Gini is the most affected by changes in inclination, whilst Smoothness and Asymmetry only vary a little. This no longer holds true for $i \geq 70^\circ$, as is shown in [Figure B5](#) for our fiducial density threshold and resolution. At these large inclinations, the galaxies appear more symmetric and there are no longer any statistically significant correlations between the non-parametric morphological indicators. Furthermore, there is more overlap between the galaxy sub-sets simulated with different physics in Asymmetry and Smoothness, compared to lower inclinations.

This paper has been typeset from a \LaTeX file prepared by the author.

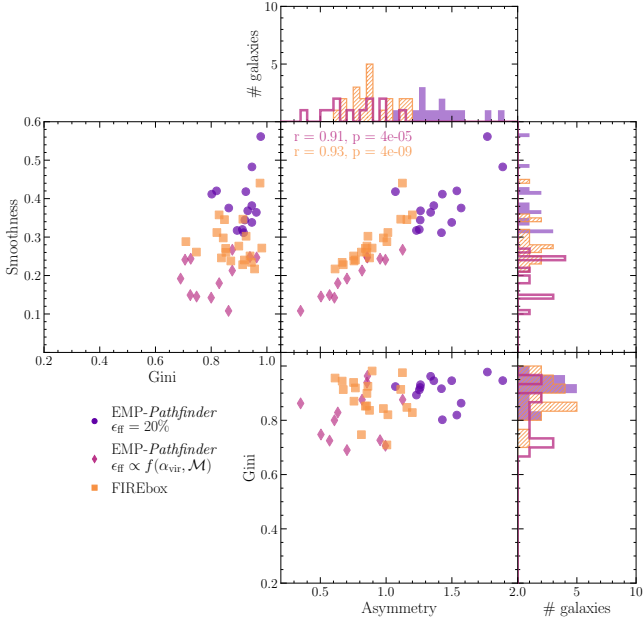


Figure B1. HI morphology as classified by the non-parametric morphological indicators Smoothness, Gini and Asymmetry (plotted against each other in the three main panels), measured from face-on HI surface density projections of the galaxies with a resolution of 80 pc and column density threshold of $3 \times 10^{20} \text{ cm}^{-2}$. Purple circles denote the *Pathfinder*-cSFE galaxies, while magenta diamonds denote the *Pathfinder*-mffSFE galaxies, and orange squares denote the FIREbox galaxies. Histograms show the marginal distributions for each indicator and galaxy sub-set. If a statistically significant correlation between two non-parametric morphology indicators is present, the Spearman rank correlation coefficient and p -value are included in the panels, colour indicating which simulated galaxy sub-set they apply to. The galaxies simulated with different sub-grid physics occupy distinctly different parts of the Asymmetry-Smoothness parameter space.

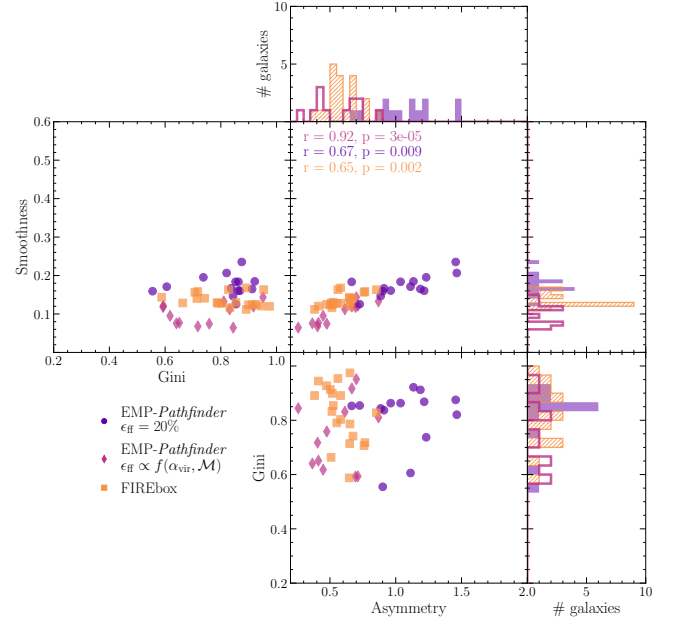


Figure B2. HI morphology as classified by the non-parametric morphological indicators Smoothness, Gini and Asymmetry (plotted against each other in the three main panels), measured from face-on HI surface density projections of the galaxies with a resolution of 500 pc and column density threshold of $7 \times 10^{19} \text{ cm}^{-2}$. Purple circles denote the *Pathfinder*-cSFE galaxies, while magenta diamonds denote the *Pathfinder*-mffSFE galaxies, and orange squares denote the FIREbox galaxies. Histograms show the marginal distributions for each indicator and galaxy sub-set. If a statistically significant correlation between two non-parametric morphology indicators is present, the Spearman rank correlation coefficient and p -value are included in the panels, colour indicating which simulated galaxy sub-set they apply to. The galaxies simulated with different sub-grid physics occupy distinctly different parts of the Asymmetry-Smoothness parameter space.

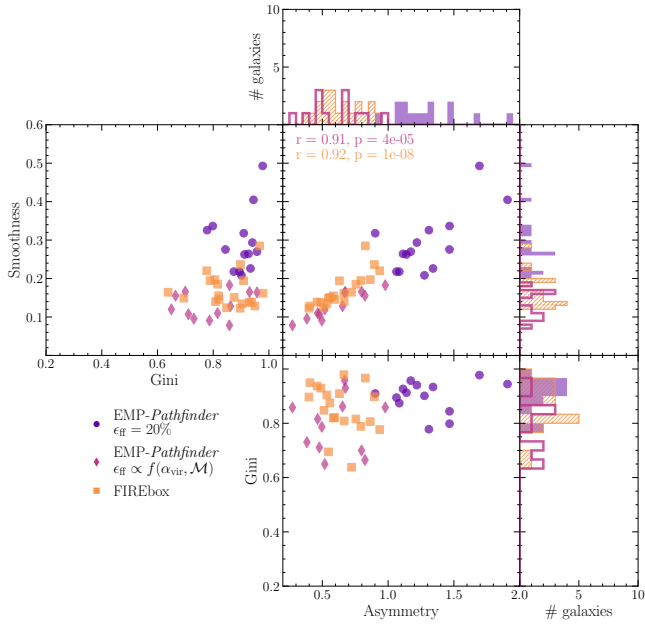


Figure B3. HI morphology as classified by the non-parametric morphological indicators Smoothness, Gini and Asymmetry (plotted against each other in the three main panels), measured from face-on HI surface density projections of the galaxies with a resolution of 500 pc and column density threshold of $3 \times 10^{20} \text{ cm}^{-2}$. Purple circles denote the *Pathfinder*-cSFE galaxies, while magenta diamonds denote the *Pathfinder*-mffSFE galaxies, and orange squares denote the FIREbox galaxies. Histograms show the marginal distributions for each indicator and galaxy sub-set. If a statistically significant correlation between two non-parametric morphology indicators is present, the Spearman rank correlation coefficient and p -value are included in the panels, colour indicating which simulated galaxy sub-set they apply to. The galaxies simulated with different sub-grid physics occupy distinctly different parts of the Asymmetry-Smoothness parameter space.

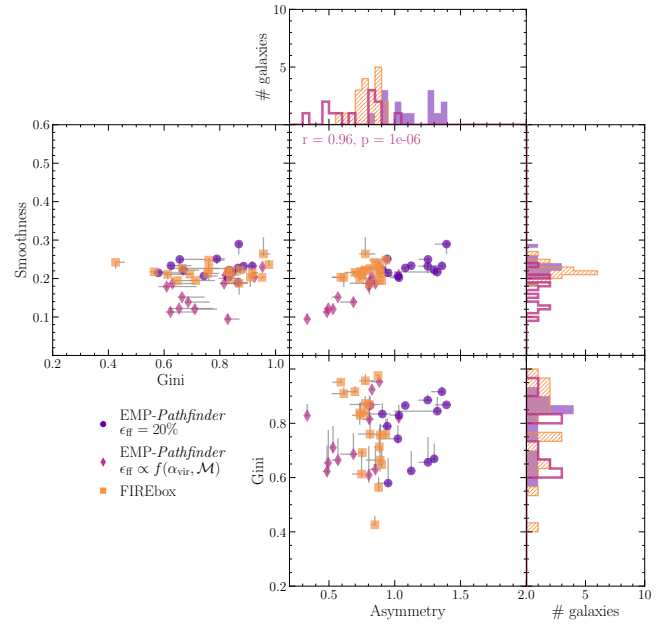


Figure B4. HI morphology as classified by the median non-parametric morphological indicators Smoothness, Gini and Asymmetry (plotted against each other in the three main panels), measured from face-on HI surface density projections of the galaxies with a resolution of 80 pc and column density threshold of $7 \times 10^{19} \text{ cm}^{-2}$ and inclinations $< 70^\circ$. Purple circles denote the *Pathfinder*-cSFE galaxies, while magenta diamonds denote the *Pathfinder*-mffSFE galaxies, and orange squares denote the FIREbox galaxies. Histograms show the marginal distributions for each indicator and galaxy sub-set. Error bars range from the minimum to the maximum of each non-parametric morphological indicator, for the inclinations considered. If a statistically significant correlation between two non-parametric morphology indicators is present, the Spearman rank correlation coefficient and p -value are included in the panels, colour indicating which simulated galaxy sub-set they apply to. The galaxies simulated with different sub-grid physics occupy distinctly different parts of the Asymmetry-Smoothness parameter space.

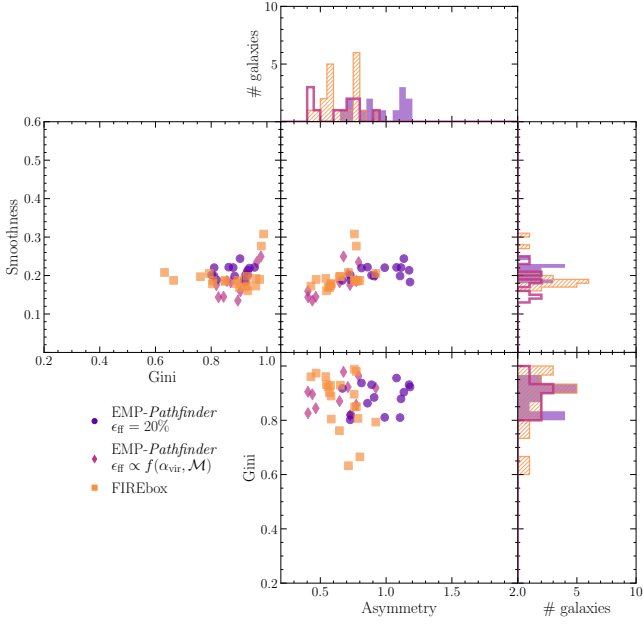


Figure B5. HI morphology as classified by the median non-parametric morphological indicators Smoothness, Gini and Asymmetry (plotted against each other in the three main panels), measured from HI surface density projections of the galaxies with a resolution of 80 pc and column density threshold of $7 \times 10^{19} \text{ cm}^{-2}$ and inclination $i = 70^\circ$. Purple circles denote the *Pathfinder*-cSFE galaxies, while magenta diamonds denote the *Pathfinder*-mffSFE galaxies, and orange squares denote the FIREbox galaxies. Histograms show the marginal distributions for each indicator and galaxy sub-set. No statistically significant correlations between two non-parametric morphology indicators are present. Galaxies appear more symmetric at high inclinations and the overlap between the different physics sub-sets increases significantly.